Declaration

I, Nemudzivhadi Hulisani (11627896), hereby declare that this dissertation titled "Computational study of low index surface of an anatase TiO_2 doped with ruthenium (Ru) and strontium (Sr) for application in Dye sensitized solar cells'' is my own work. This dissertation has not been submitted for a degree at any other university. All the reference materials contained have been acknowledged.

Signed by:……at……

Date:…….

Acknowledgments

I would like to thank God for enabling me to complete this mini dissertation and helped strengthened me throughout my studies. I would love to extent my utmost gratitude to my supervisor Dr N.E Maluta and co-supervisor Prof R.R Maphanga for helping me out throughout this research. I would also like to extent my gratitude to the department of physics at the University of Venda for the opportunity to proceed with my master studies. Lastly, I would like to thank my colleague Mr R.S Dima and others for their support. Also not forgetting to thank the financial support from National Research Foundation (NRF). The Centre for High Performance Computing (CHPC) is acknowledged for using their computing facilities to carry out this research.

Abstract

Titanium dioxide (TiO_2) is considered to be an ideal semiconductor for photocatalysis because of its high stability, low cost and safety towards both humans and the environment. Doping TiO_2 with different elements has attracted much attention as the most important way of enhancing the visible light absorption, in order to improve the efficiency of the dye sensitized solar cells (DSSCs). In this study, first principle density functional theory was used to investigate electronic and optical properties of bulk anatase TiO_2, undoped, and ruthenium (Ru) and strontium (Sr) doped anatase TiO_2 (1 0 0) surface. Two different doping approaches i.e., substitutional and adsorption mechanisms were considered in this study. The results showed that absorption band edges of Ru and Sr-doped anatase TiO_2 (1 0 0) surface shift to the long wavelength region compared to the bulk anatase TiO_2 and undoped anatase TiO_2 (1 0 0) surface. Also, the results revealed that the band gap values and the carrier mobility in the valence band, conduction band and impurity energy levels have a synergetic influence on the visible-light absorption and photocatalytic activity of the doped anatase TiO_2 (1 0 0) surface. Furthermore, according to the calculated results, we propose the optical transition mechanisms of Ru and Sr-doped anatase TiO_2 (1 0 0) surface. Thus, we conclude that the visible light response of TiO_2 can be modulated by doping with both Ru and Sr. However, Sr-doped system shows higher photocatalytic activity than the Ru-doped system. The study has successfully probed the interesting optical response mechanism of TiO_2 (1 0 0) surface.

Keywords: Doping, anatase TiO_2, low index surface, first principle density functional theory, electronic properties, optical properties, photocatalytic activity.

List of Figures

Figure 1.1 Cumulative installed solar PV globally……2
Figure 1.2 Simple illustration of converting solar energy to electrical energy using solar panels……3
Figure 1.3 Schematic view of a DSSCs……6
Figure 1.4 Efficiency of emerging PV versus time……8
Figure 1.5 The crystal structures of rutile, brookite and anatase TiO_2……10
Figure 2.1 Semiconductor band gap of anatase TiO_2……15
Figure 2.2 Direct and indirect band gap……16
Figure 2.3 Photograph of red TiO_2 and UV-visible absorption spectra of white TiO_2 and red TiO_2……18
Figure 2.4 Density of states plots for (1 0 1) and (0 0 1) surface of anatase TiO_2 and surface heterojunction……21
Figure 3.1 Flowhart of electronic structure methods used for solving Kohn-Sham equations……27
Figure 3.2 Schematic of the smoothing effect of the pseudo-wavefunction and potential compared to the all-electron versions……33
Figure 4.1 Total energy vs kinetic energy cut-off for anatase TiO_2……38
Figure 4.2 Total energy vs number of k-points of anatase TiO_2……39
Figure 4.3 Band structure and density of states of anatase TiO_2 bulk structure……41
Figure 4.4 Calculated real and imaginary parts of dielectric function, refractive index and extinction coefficient……43
Figure 4.5 Reflectivity and loss function of bulk anatase TiO_2……44
Figure 4.6 The absorption coefficient of bulk anatase TiO_2 against wavelength and photon energy……45
Figure 4.7 Cleaved (1 0 0) low index surface from anatase TiO_2……46
Figure 4.8 Structure of Ru-doped anatase TiO_2 (1 0 0) surface by replacing one Ti atom with Ru and adsorbing Ru atom inside and on top of the surface……47

Figure 4.9 Structure of Sr-doped anatase TiO_2 (1 0 0) surface by replacing one Ti atom with Sr and adsorbing Sr atom inside and on top of the surface……48
Figure 4.10 Band structure and density of states of undoped anatase TiO_2 (1 0 0) surface under the scissor operation……48
Figure 4.11 Band structure of Ru and Sr-doped anatase TiO_2 (1 0 0) surface by replacing one Ti with dopant atoms under the scissor operation……...51
Figure 4.12 Band structure of Ru and Sr-doped anatase TiO_2 (1 0 0) surface by adsorbing dopant atoms on top of the surface under the scissor operation……..52
Figure 4.13 Band structure of Ru and Sr-doped anatase TiO_2 (1 0 0) surface by adsorbing dopant atom in the surface under the scissor operation……52
Figure 4.14 DOS of Ru and Sr-doped anatase TiO_2 (1 0 0) surface by replacing one Ti with dopant atoms under the scissor operation.……54
Figure 4.15 DOS of Ru and Sr-doped anatase TiO_2 (1 0 0) surface by adsorption dopant atoms on top of the surface under the scissor operation……55
Figure 4.16 DOS of Ru and Sr-doped anatase TiO_2 (1 0 0) surface by adsorption dopant atoms in the surface under the scissor operation.……55
Figure 4.17 The absorption coefficient of undoped and substitutional Ru- and Sr-doped anatase TiO_2 (1 0 0) surface…….....57
Figure 4.18 The absorption coefficient of undoped and Ru- and Sr-doped anatase TiO_2 (1 0 0) surface by dopant atoms on top of the surface……...58
Figure 4.19 The absorption coefficient of undoped and Ru- and Sr-doped anatase TiO_2 (1 0 0) surface by dopant atoms in the surface……58
Figure 4.20 Loss function and reflectivity of undoped and Ru- and Sr-doped anatase TiO_2 (1 0 0) surface by substitution…….....61
Figure 4.21 Loss function and reflectivity of undoped and Ru- and Sr-doped anatase TiO_2 (1 0 0) surface by dopant atoms in the surface……61
Figure 4.22 Loss function and reflectivity of undoped and Ru- and Sr-doped anatase TiO_2 (1 0 0) surface by dopant atoms on top of the surface……62
Figure 4.23 Imaginary part of dielectric function and real part of refractive index of undoped and Ru- and Sr-doped anatase TiO_2 (1 0 0) surface by substitution……64

Figure 4.24 Imaginary part of dielectric function and real part of undoped and Ru- and Sr-doped anatase TiO_2 (1 0 0) surface by on top adsorption……65
Figure 4.25 Imaginary part of dielectric function and real part of refractive index of undoped and Ru- and Sr-doped anatase TiO_2 (1 0 0) surface by in-surface adsorption……65

List of tables

Table1.1 Comparison between semiconductors based solar cells and the DSSCs……5

Table 1.2 The summary of bulk properties of TiO_2……9

Table 4.1. Optimized structural parameters of bulk anataseTiO_2……..40

Table 4.2 Comparison of the calculated energy band gaps (eV) and scissor operator (1.107 eV) of Ru- and Sr-doped anatase TiO_2 (1 0 0) surface modelled by two approaches……..50

Table of Contents

Chapter 1 1

1. Introduction 1

1.1 Solar energy 1

1.2 Solar photovoltaic technologies 3

1.2. Background 6

1.2.1 Dye-sensitized solar cells 6

1.2.2 Efficiency of dye sensitized solar cells 7

1.2.3 Titanium dioxide 8

1.2.4 Anatase TiO_2 10

1.2.5 Ruthenium and strontium 11

1.3. Purpose of the study 12

1.3.1 Aim 12

1.3.2 Objectives of the research 12

Chapter 2 14

2. Literature review 14

2.1 Anatase TiO_2 band gap 14

2.2 Doping of anatase TiO_2 17

2.3 Anatase TiO_2 low index surfaces 19

Chapter 3 23

3. Methodology 23

3.1 Density Functional Theory 23

3.1.1 Local Density Approximation 27

3.1.2 Generalized Gradient Approximation 28

3.2 Plane-wave pseudopotential method 28

3.2.1 Plane-wave basis 29
3.2.2 The pseudopotential method 31
3.2.3 Brillouin zone sampling 33
3.2.4 Convergence tests 34
3.3 Computer code 35
3.3.1 Cambridge Serial Total Energy Package 35
3.3.2 Computational details 35
CHAPTER 4 37
4. Results and discussions 37
4.1 Convergence test for bulk anatase TiO_2 37
4.2 Bulk anatase TiO_2 38
4.2.1 Structural properties 38
4.2.2 Electronic properties 40
4.2.3 Optical properties 41
4.3 Anatase TiO_2 (1 0 0) surface 45
4.3.1 Ru and Sr-doped anatase TiO_2 (1 0 0) surface 46
4.4 Electronic properties 47
4.4.1 Band structure and DOS of undoped anatase TiO_2 (1 0 0) surface 47
4.4.2 Band structure of Ru and Sr-doped anatase TiO_2 (1 0 0) surface 48
4.4.3 DOS of Ru- and Sr-doped anatase TiO_2 (1 0 0) surface 53
4.5 Optical properties of Ru and Sr-doped anatase TiO_2 (1 0 0) surface 55
4.5.1 Optical absorption 56
4.5.2 Reflection and energy loss function 59
4.5.3 Dielectric function and refractive index 61
Chapter 5 66

5. Conclusion 66

References 68

Chapter 1

1. Introduction

1.1 Solar energy

Energy is the basic resource of today's world. Along with the increase of the population, the demand of the amount of energy resource is increasing rapidly. The solution to the growing energy demand and alternative environmentally sustainable energy resources in the world might lie in the ability to capture and utilize solar energy. Solar energy can help world to meet their sustainable development goals through provision of access to clean, secure, reliable and affordable energy. To capture and utilize solar energy for a sustainable development on a larger scale, development of cheaper technologies is regarded as an added advantage. Solar energy as one of the most promising green energy source has become a hot spot in both academia and industrial research [1].

The earth receives an incredible supply of solar energy from the sun. The sun and an average star are a fusion reactor that have been burning for over 4 billion years. The sun provides enough energy in one minute to supply the world's energy needs for one year. In one day, it provides more energy than our current population would consume in 27 years [1]. The amount of solar radiation striking the earth over a three-day period is equivalent to the energy stored in all fossil energy sources. Since the 18th century solar thermal collector has been introduced and it has proved difficult to capitalize on this huge amount of solar energy. The first ever solar thermal collector was invented by a Swiss scientist, Horace de Saussure in 1767. Robert Stirling built heat engines, which were used by Lord Kelvin on his university classes in 1816. This engine was later used in the dish/Stirling system, a solar thermal electric technology that concentrates the sun's thermal energy in order to produce power. Producing the electricity directly from solar energy was the second discovery. This technology was discovered by French physicist Alexander Edmond Becquerel in 1839, who discovered the photovoltaic effect while experimenting with an electrolytic cell made up of two metal electrodes placed in an electricity conducting solution and electricity generation increased when exposed to light, that marked the beginning of the solar cell's technology [2].

The worldwide growth of solar photovoltaics (PV) has been fitting an exponential curve for more than two decades. During this period of time PV has evolved from a pure niche market of small-scale applications towards becoming a mainstream electricity source. When solar PV systems were first recognized as a promising renewable energy technology, programs such as feed-in tariffs were implemented by a number of governments in order to provide economic incentives for investments [3]. Figure 1.1 below shows the cumulative installed solar PV globally from 2000 to 2015.

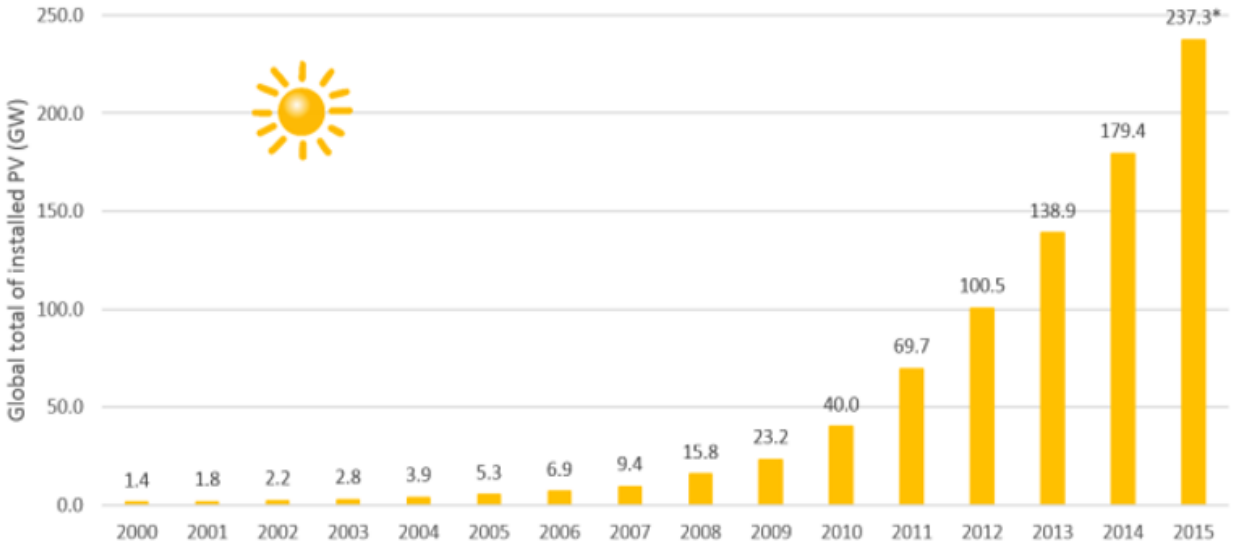

Figure 1.1 Cumulative installed solar PV globally [4].

In solar cells technology, sunlight is composed of photons or particles of solar energy. These photons contain various amounts of energy corresponding to the different wavelengths of the solar spectrum. When photons strike a photovoltaic cell, they may be reflected, pass right through, or be absorbed. Only the absorbed photons provide energy to generate electricity. When enough sunlight (energy) is absorbed by the material (a semiconductor), electrons are dislodged from the material's atoms. Special treatment of the material surface during manufacturing makes the front surface of the cell more receptive to free electrons, so the electrons naturally migrate to the surface.

When the electrons leave their position, holes are formed. When many electrons, each carrying a negative charge, travel toward the front surface of the cell, the resulting

imbalance of charge between the cell's front and back surfaces creates a voltage potential like the negative and positive terminals of a battery. When the two surfaces are connected through an external load, electricity flows as illustrated in Figure 1.2.

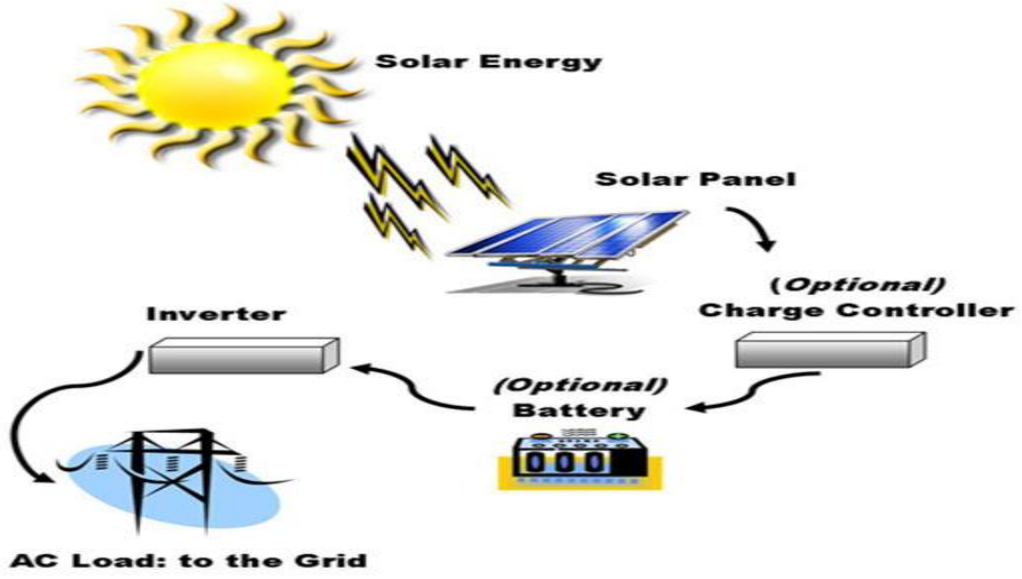

Figure 1.2 Simple illustration of converting of solar energy to electrical energy using solar panels.

1.2 Solar photovoltaic technologies

PV is an environmental-friendly technology currently available and it uses semiconductor material to convert light to electricity [2]. Solar PV technologies are small and highly modular, which can be used virtually anywhere, unlike many other electricity generation technologies. It is one of the fastest growing renewable energy technologies, projected to play a major role in the future global electricity generation [5]. The added advantage of the PV systems as a renewable energy technology, is that their modular size is within the reach of individuals, co-operatives and small-businesses enabling them to access and generate their own electricity and also play a role in mitigating climate change.

PV cell technologies are usually classified into three generations, depending on the basic material used and the level of commercial maturity. The first generation is composed of solar cells that are relatively expensive to produce and have a high efficiency [2]. The second generation is composed of types of solar cells that have an even lower efficiency, but are much cheaper to produce, such that the cost per Watt is lower than that of first-

generation cells, because they are based on amorphous silicon [2]. Due to high costs of first-generation solar cells, toxicity and limited availability of materials for second-generation solar cells, a new generation of solar cells emerged. Currently there is a lot of research going on in what is being referred to in the industry as third generation solar cells. The third generation refers to the solar cells that are very efficient [2]. Most technologies for 3rd generation are not yet commercialized, however there is a tremendous research activity in this area. The ultimate goal for the research is to develop third generation solar cells that are cheaper to produce by designing cheaper materials with optimal efficiency. In the next paragraphs, 3rd generation solar cells are discussed in detail.

Third-generation PV technologies are at the pre-commercial stage and vary from technologies under demonstration to novel concepts still in need of basic research and development. Some of those PV technologies are beginning to be commercialized, but it remains to be seen how successful they will be in taking market share from existing technologies [2].

There are four types of third-generation PV technologies:

(i) Nanocrystal based solar cells

(ii) Polymer based solar cells

(iii) Dye sensitized solar cells

(iv) Concentrated solar cells.

These are the novel technologies that are promising but not commercially proven yet. Most developed third generation solar cell types are dye sensitized and concentrated solar cells. Dye-sensitized solar cells (DSSCs) are frequently called Grätzel cells, named after the developer. DSSCs separate the absorption of photons from the energy generation. Among various solar cells, DSSCs demonstrate specific advantages over other photovoltaic devices; because of their high efficiency, low cost, simple fabrication procedures, environmental friendliness, transparency, and good plasticity. Though DSSCs perform well under laboratory conditions relative to other solar cells, parameters

such as efficiency, lifetime, and cost determine their commercial applications. The major components of conventional DSSCs include a nanocrystalline semiconductor oxide, a dye sensitizer, a redox electrolyte, and a counter electrode. DSSCs has emerged as a new class of low-cost energy conversion devices with simple manufacturing procedures. It has been shown that DSSCs are promising class of low cost and moderate efficiency solar cell. General comparison between semiconductor based solar cells and DSSCs is presented in Table 1.1.

Table1.1 Comparison between semiconductors based solar cells and the DSSCs [6].

	Semiconductor solar cells	DSSCs
Transparency	Opaque	Transparent
Material and process	Normal	Great
Power generation cost	High	Low
Power generation efficiency	High	Normal
Colour	Limited	Various

In fact, in a semiconductor p-n junction solar cell charge separation is taken care by the junction built in electric field, while in DSSCs charge separation is by kinetic competition as in photosynthesis [6]. In addition to their unique electronic properties, TiO_2 nanostructures function as semiconductor material in the DSSCs. The working principle of DSSCs substantially differs from that of a conventional solar cell based on silicon. In silicon, a *p-n* junction is obtained by joining semiconductors of different charge carriers' concentration in a very close contact. In this case, the processes of light absorption and charge transport are caused in the same material [7].

Concentrated PV solar cell is another promising technology. Main principle of concentrated cells is to concentrate large amount of solar radiation on to a small region where the PV cell is located. The amount of semiconductor material, which might be very expensive, is reduced in this way. In such systems, a perfect optical system should be

integrated. Concentration levels start from ten suns to thousands of suns and the total cost can be lower than conventional systems [4].

1.2. Background

1.2.1 Dye-sensitized solar cells

DSSCs were discovered by Grätzel *et al*. in 1991 and have since attracted considerable research interest due to their low cost, ease of fabrication and environmental friendliness [6,8,9]. They form a sandwich-like structure with the dye molecule or photosensitizer playing a pivotal role through its ability to absorb visible light photons. Subsequently, a significant amount of research on DSSCs has been focused on designing and optimizing the photosensitizer to absorb a wide spectrum of wavelengths and increase the efficiency of the solar energy conversion [10,11].

DSSCs are composed of four major components: a nanostructured material, ideally semiconductor which is typically TiO_2; a monolayer of dye-sensitizer to absorb light; an electrolyte for dye regeneration, which creates the interface with the semiconductor and a counter electrode carrying an electrocatalyst, which facilitates transfer of electrons to the electrolyte as illustrated in Figure 1.3.

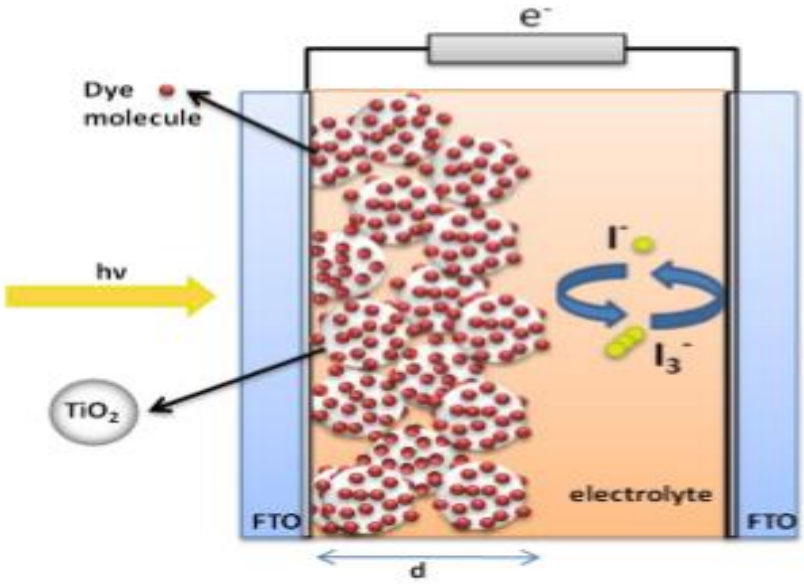

Figure 1.3 Schematic view of a DSSCs [12].

Nearly all the components of a DSSCs are tenable. Up to now the most successful combination of materials is still the one reported in the pioneering work by the Grätzel group [8], which opened the research field of DSSCs. The anode DSSCs is transparent like glass so that sunlight can be absorbed by the inner parts of the solar cell (see Figure 1.3). Between the anode and the cathode is a mush of TiO_2 nanoparticles that act like a roadway for the electrons (electricity) coursing through the cell. An electrolyte (usually iodide) fills the spaces between the TiO_2 nanoparticles and helps transfer electrons from the cathode to the dye molecules (after the dye releases an electron it needs another to replace the one it lost). On the other end of the cell is the cathode, typically a film of graphite or platinum. The anode sends electrons from the solar cell through a wire to the device that the cell is powering, then electrons loop back to the cathode [12].

TiO_2 has been widely applied in DSSC systems because of its stability, low cost and environmental friendliness, but has a wide band gap [13]. The high band gap of TiO_2 crucially limits its practical application involving the photons absorption and electrons transport in DSSCs [14]. To enhance the efficiency of DSSCs reduction of TiO_2 band gap is required such that the absorption properties will match well with visible solar spectrum [14,15]. Thus, the modification of electronic structure and the related properties for TiO_2 plays a vital role in understanding the dye uptake on DSSCs. In the current study, computer simulation methods will be used to understand electronic and optical properties of Ru and Sr doped on low index (1 0 0) surface of anatase TiO_2.

Previous literature have shown that there are still gaps on understanding the behavior of TiO_2 as a material for DSSCs [14-16], and further investigations are required. The required areas of study include understanding how dye uptake happens in solar cell and electron transport among others. Most literature has focused on investigating rutile polymorph of TiO_2 as semiconductor material for DSSCs. In this study, anatase polymorph of TiO_2 will be investigated for potential application in DSSCs.

1.2.2 Efficiency of dye sensitized solar cells

The efficiency of DSSCs has continued to increase in the last 20 years, with a confirmed record of 14.1% achieved by G24 Power advisory board member Professor Michael Grätzel and his team at École Polytechnique Fédérale de Lausanne (EPFL) [17]. Figure

1.4 below shows efficiency of emerging PV technologies versus time, DSSCs show increased efficiency over time as calculated by various research groups.

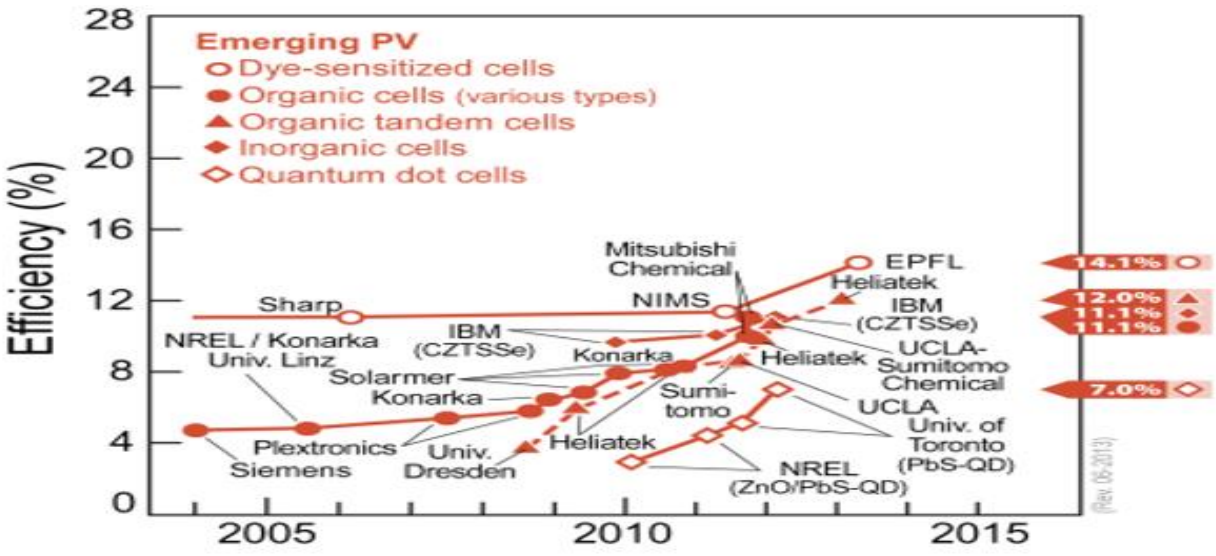

Figure 1.4 Efficiency of emerging PV versus time [17].

1.2.3 Titanium dioxide

TiO_2 is a white solid inorganic substance, that is thermally stable, non-flammable and poorly soluble. Titanium occurs naturally in several kinds of rock and mineral sands. Titanium is the ninth most common element in the earth's crust [18]. TiO_2 is typically thought of as being chemically inert. It has been used for many years in a vast range of industrial and consumer goods including paints, coatings, adhesives, paper, paperboard, plastics, rubber, printing inks, coated fabrics, textiles, catalyst systems, ceramics, floor coverings, roofing materials, cosmetics, pharmaceuticals, water treatment agents, food colorants, in automotive products and others [18].

TiO_2 is used in heterogeneous catalysis, as a photocatalyst in solar cells to produce hydrogen and electric energy, as gas sensor, as a corrosion-protective coating, as an optical coating in ceramics and in electric devices [18]. A better understanding and improvement of catalytic reaction is one main driving force for surface investigations on TiO_2. Because most heterogeneous catalysts consist of small metal clusters on an oxide support, numerous studies of metals growth on TiO_2 were performed [18,19]. These metal

TiO_2 systems often serve as a model for other metal oxide surfaces. Traditionally, TiO_2 is a component in mixed vanadia/titania catalysts used for selective oxidation reactions [20]. TiO_2 nanomaterials (ultrafine) are transparent and more effective as ultraviolet (UV) absorbers or photocatalysts. The transparency and UV absorbance allow for effective use as a protective ingredient for sunscreens. TiO_2 is considered very close to an ideal semiconductor for photocatalysis because of its high stability, low cost and safety towards both human beings and environment. It is an environmentally-free material with unique optical and electrical properties, good chemical stability, high photoactivity and a large band gap [13-22]

TiO_2 has three commonly known polymorphs, which are rutile, anatase and brookite. These crystalline forms of TiO_2 occur in nature as minerals, but only rutile and anatase can be synthesized in pure form at low temperature until recently [23]. Hence, the anatase and rutile phases which belong to the tetragonal crystal system are widely studied for their syntheses, characterizations and photocatalytic properties [23]. So far, the anatase phase is known to exhibit higher photocatalytic efficiency compared to the rutile phase. Little efforts have been made on synthesis, characterization and properties of brookite phase which belongs to the orthorhombic crystal system [22,23].

Table 1.2 The summary of bulk properties of TiO_2 polymorphs [20].

Crystal structures	Density (kg/m^3)	Standard heat capacity, C^0_P, 298.15j (mol ^oC)	Band gap (eV)	Refractive index		
				n_g	n_m	n_p
Rutile	4240	55.06	3.0 (indirect)	2.947	-	2.651
Anatase	3830	55.52	3.2 (indirect)	2.568	-	2.658
Brookite	4170	-	-	2.809	-	2.667

The crystal structure of TiO_2 polymorphs can be explained by the different spatial arrangements of TiO_6 octahedra (Ti^{4+} ions bordered by six O^{2-} ions) [20]. The differences between the three crystal structures are the various degrees of distortion and 3-D assembly of the TiO_6 octahedra as illustrated in Figure 1.5. For anatase tetragonal crystal structure ($a = b = 3.78$ Å, $c = 9.50$ Å), each octahedron shares corners to form (0 0 1) planes. The tetragonal structure of rutile ($a = b = 4.58$ Å, $c = 2.95$ Å), on the other hand consists of edge sharing octahedrons forming the (0 0 1) planes. The orthorhombic structure of brookite phase ($a = 5.43$ Å, $b = 9.16$ Å, $c = 5.13$ Å) is composed of both corner and edge sharing octahedra. These different crystal structures result in various densities and electronic structures of the three TiO_2 polymorphs. The grey spheres represent titanium atoms while the red spheres represent oxygen atoms in Figure 1.5.

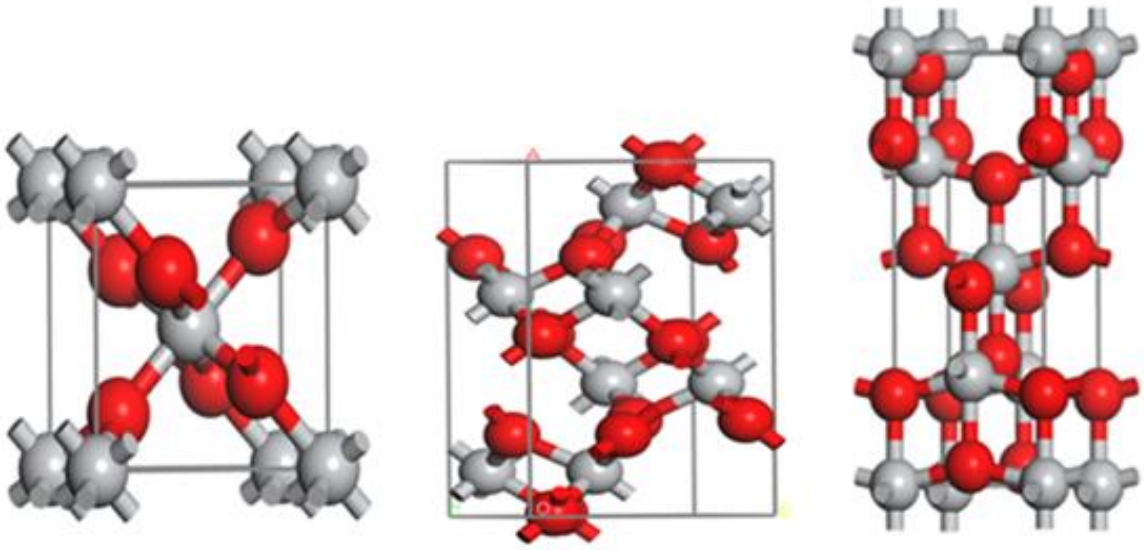

Figure 1.5 The crystal structures of rutile, brookite and anatase TiO_2.

1.2.4 Anatase TiO_2

From the three TiO_2 polymorphs, anatase has been widely used as a popular catalyst, because of its various merits, such as optical and electronic properties, high photocatalytic activity, low cost, non-toxicity and chemical stability [20- 22]. It has been found that anatase has widespread technological applications in nanostructured solar cells and spintronic devices. Also anatase is one of the most popular and promising materials in photocatalytic applications due to the strong oxidizing power of its holes, high

photo stability and redox selectivity [24]. But both polymorphs rutile, anatase and brookite have high refractive indices, which result in high reflectivity from the surfaces. Consequently, Ti particle size and correspondingly high surface areas are used owing to their resultant pacifying power and brightness. However, paints utilize polymeric binders to fix the pigment and, when in contact with Ti, the polymer may oxidize when exposed to sunlight. This effect is known as chalking and in addition to the direct degrading effect of UV radiation, is accelerated by the photocatalytic activity of TiO_2, which also is enhanced by the high surface area of this material [24].

Anatase is always found as small, isolated and sharply developed crystals, like rutile, a more commonly occurring polymorph of TiO_2. The anatase TiO_2 system crystallizes into the tetragonal system, although the degree of symmetry is the same, there is no relation between the interfacial angles of the anatase and rutile, except in the prism-zone of 45° and 90° [20]. It is metastable, but it can be kinetically stabilized at lower temperatures. Anatase is often the product phases in the synthesis of TiO_2 owing to its less constrained structure and consequent enhanced kinetics of formation. The phase transformation kinetically stabilized anatase to thermodynamically stable, while rutile does not have a distinct transformation temperature [25].

1.2.5 Ruthenium and strontium

Ruthenium is a chemical element with symbol Ru and atomic number 44. It is a rare transition metal belonging to the platinum group of the periodic table. Like the other metals of the platinum group, Ru is inert to most other chemicals [26]. Initially ruthenium-based complexes had received interest as photo sensitizers due to their favourable photo electrochemical properties and high stability in the oxidized state [26]. Ruthenium (II)-based dyes in conjunction with iodide-based electrolytes have successfully been employed to achieve maximum power conversion efficiency (PCE) of 11.9% [27,28]. The scarcity of noble metals and high cost of Ru dyes, however limit their large-scale commercialization [27,28].

Strontium is a chemical element with symbol Sr and atomic number 38. It is alkaline earth metal (AEM), soft silver-white or yellowish metallic element that is highly reactive chemically [29]. The metal turns yellow when it is exposed to air. Strontium has physical

and chemical properties like those of its two vertical neighbors, calcium and barium. It occurs naturally in the minerals celestine, putnisite and strontianite. While natural strontium is stable, the synthetic strontium-90 (90Sr) isotope is present in radioactive fallout and has a half-life of 28.90 years [29]. The strontium in group two has two electrons in its valence shells. This enables the metal to easily loss the electrons which increases their stability and allows them to form the compounds. Both Ru and Sr are divalent elements as they have two electrons in their outermost energy levels. Therefore, Ru and Sr are structurally very similar to the high-temperature cuprite superconductors [30,31].

Due to their simple fabrication and potential low production costs, the DSSCs are attractive photovoltaic technology for mass production. The main challenge with these types of solar cells is an overall conversion efficiency which is about 14.1% [17]. The low conversion efficiency of DSSCs is closely related to the wide band gap of TiO_2 semiconductor. The band gap acts as recipient of the electrons injected from the photon excited dye. In this study, the focus is on understanding the surface interaction between the TiO_2 surfaces with and Ru and Sr elements in order to understand factors affecting the efficiency of DSSCs using computational simulation method. Ru and Sr atoms are adsorbed on anatase TiO_2 (1 0 0) low index surface, to understand the optical and electronic properties.

1.3. Purpose of the study

1.3.1 Aim

The aim of this study was to use computational modeling techniques, to investigate the optical and electronic properties of TiO_2 (1 0 0) low index surface doped with Ru and Sr atoms for application in dye sensitized solar cells.

1.3.2 Objectives of the research

Objectives of this study were to:

- determine the convergence parameters (that is, energy cut-off and k points) for anatase TiO_2.
- optimize the bulk structure for anatase TiO_2 using geometry optimization technique.

- cleave the (1 0 0) low index surface from anatase TiO_2.
- calculate properties for cleaved low-index surfaces.
- dope the surface with Ru and Sr.
- calculate electronic density of states and band structure for doped surface and compare the band gaps of undoped and doped surface.
- calculate optical properties (i.e., absorbance, reflectance, refractive index).

Chapter 2

2. Literature review

2.1 Anatase TiO_2 band gap

The band gap of a semiconductor is the minimum energy required to excite an electron that is stuck in its bound state into a free state where it can participate in conduction. Figure 2.1 illustrated band structure of a semiconductor which gives the energy of the electrons on the y-axis. The lower energy level of a semiconductor is called the valence band (VB), while the energy level at which an electron can be considered free is called the conduction band (CB) [32]. The band gap is the gap in energy between the VB and CB (see Figure 2.1).

The absorption properties, especially the absorption in visible region, are very important for PV materials [33]. Low band gap materials are of interest because their absorption spectra cover from the visible region to the near-infrared region [34]. Figure 2.1 depicts the experimental band gap of anatase TiO_2, where the VB is composed of O-2p orbitals and CB is composed of Ti-3d orbitals, with the wavelength less than 390 nm and the band gap of 3.2 eV [35]. When the band gap of TiO_2 is reduced, the wavelength will increase and shift to the visible region or infrared. The electron becomes excited into the CB, it is free to move on the semiconductor and participate in conduction. However, the excitation of an electron to the CB will also allow an additional conduction process to take place, as it leaves behind an empty space for an electron. An electron from a neighbouring atom can move into this empty space. When this electron moves, it leaves behind another space. The continual movement of the space for an electron, called a hole, can be illustrated as the movement of a positively charged particle through the crystal structure. Consequently, the excitation of each electron from CB to VB leaves a hole in the VB**,** the number of holes in the VB equals the number of electrons in the CB. Therefore, the process results in the creation (generation) of electron-hole pairs. Thus, both the electron and hole can participate in conduction and are called carriers.

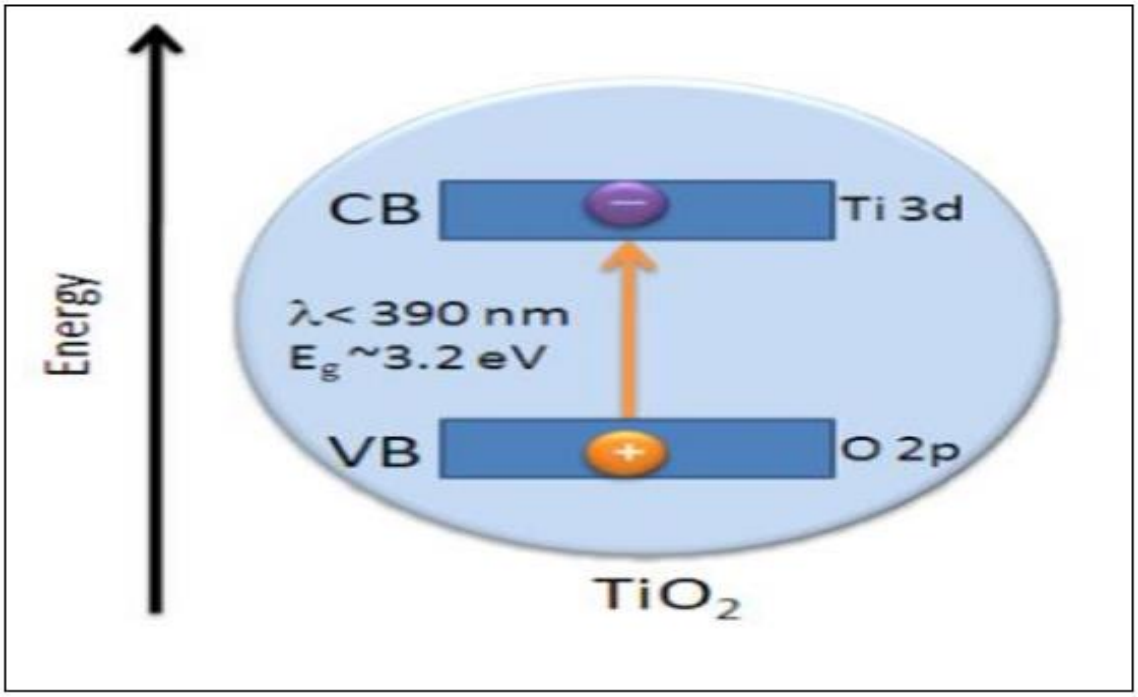

Figure 2.1 Semiconductor band gap of anatase TiO_2 [35].

In general, a material with a band gap of less than about 3.2 eV is regarded as a semiconductor. A material with a band gap of greater than 3.2 eV will commonly be regarded as an insulator. Several ceramics such as silicon carbide (SiC), TiO_2, barium titanate ($BaTiO_3$) and zinc oxide (ZnO) have band gaps around 3.2 eV. Such ceramics are often referred to as wide-band-gap semiconductors [35].

There are two band gap semiconductors, i.e as direct band gap and indirect band gap. In a direct band gap semiconductor, the top of the VB and the bottom of the CB occur at the same value of momentum (see Figure 2.2). In contrast, for an indirect band gap semiconductor, the maximum energy of the VB occurs at a different value of momentum to the minimum in the CB energy as illustrated in Figure 2.2. The difference between the two band gaps is important in optical devices.

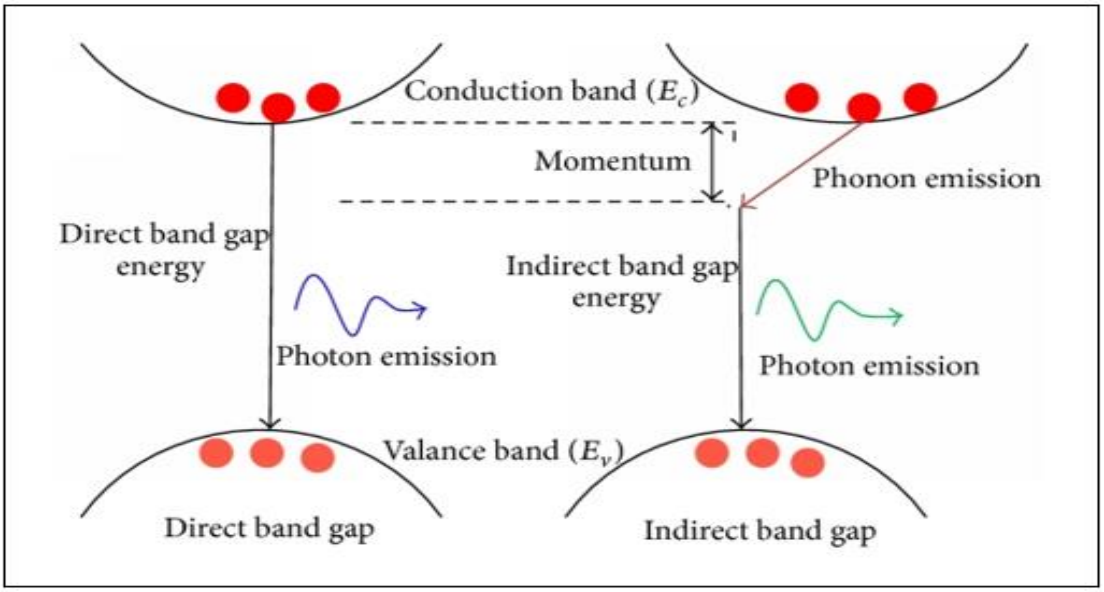

Figure 2.2 Direct and indirect band gap [35].

A photon can produce an electron-hole pair in a direct band gap semiconductor quite easily because the electron does not need to be given momentum very much. However, an electron must also undergo a significant change in its momentum for a photon of energy to produce an electron-hole pair in an indirect band gap semiconductor. This is possible, but it requires such an electron to interact not only with the photon to gain energy, but also with a lattice vibration called a phonon to either gain or lose momentum [35].

The same principle applies to recombination of electrons and holes to produce photons. The recombination process is much more efficient for a direct band gap semiconductor than for an indirect band gap semiconductor, where the process must be mediated by a phonon. Because of such considerations, many researchers have been working on gallium arsenide and other direct band gap semiconductors to make optical devices such as light-emitting diodes (LEDs) and semiconductor lasers [35].

The band gap engineering and carrier transport in anatase TiO_2 for the application in solar energy harvesting has been reported recently by Yang [32]. The study elaborated that anatase TiO_2 can been used in photocatalysis and photovoltaics because of its comprehensive combination of energy band structure, carrier transport and inertness.

Wide band gap and relative slow carrier transport, however limit its full potential in these applications. Thus, a 3.2 eV band gap of anatase indicates its low efficiency of utilizing full spectrum of solar light and band gap engineering has been shown to improve the efficiency of such solar cells [32].

2.2 Doping of anatase TiO_2

Doping is a general method of increasing visible light absorption by narrowing the band gap. Anatase TiO_2 has been widely investigated photocatalyst in the past four decades. Although doping can increase visible light absorption of anatase TiO_2, few successes of harvesting the complete spectrum of visible light is achieved [7, 11, 16]. Shenyang National Laboratory for Materials Science (SYNL) and Institute of Metal Research (IMR) have been devoted to solving the challenge of narrowing the band gap of wide-band gap semiconductors to harvest the complete spectrum of visible light. Their early studies have revealed that the spatial distribution of dopants in photocatalysts plays a vital role in determining the band gap narrowing [7, 11, 16]. Furthermore, it confirmed that layered structure is favorable for realizing homogeneous doping by providing the facile diffusion channels of dopants. For example, the homogeneous nitrogen (N) doping in layered $Cs_{0.68}Ti_{1.83}O_4$ can realize the redshift of light absorption edge by 100 nm towards visible light region. However, the effective bulk doping in non-layered photocatalysts (i.e. TiO_2) remains a challenge [36].

The results of anatase TiO_2 with a gradient of boron (B) and N dopants were red and a high absorbance in the complete spectrum of visible light as shown in Figure 2.3 [36]. The photoelectrode fabricated from the red TiO_2 has the ability of splitting water up to 700 nm, which indicates the possibility of realizing efficient visible light photocatalytic water splitting with TiO_2 based photocatalysts. The results obtained shed some light on how to effectively increase high visible light absorbance of wide-band gap photocatalysts using doping strategy [36].

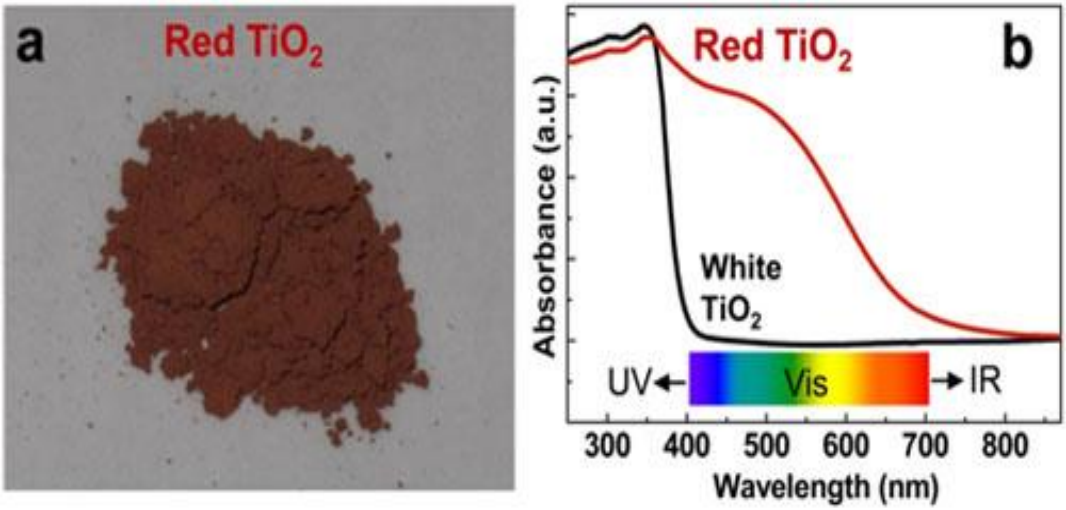

Figure 2.3 (a) Photograph of red TiO_2; (b) UV-visible absorption spectra of white TiO_2 and red TiO_2 [36].

Huang *et al*. investigated the influences of doping on photocatalytic properties of TiO_2 [37]. The findings showed that doping is an effective method of extending the light absorption to the visible light region, because anatase TiO_2 is activated under ultraviolet light irradiation due to its wide bandgap, high recombination, and weak separation efficiency of carriers. In their study, issues pertaining to the importance of doping, different doping modes, preparation method, and photocatalytic mechanism in TiO_2 photocatalysts were addressed. They investigated mechanisms for Ti^{3+} self-doping, nonmetal doping, metal doping, and co-doping. The main objective of studying photocatalytic processes, was to elucidate the mechanistic models for better understanding of the photocatalytic reactions and to derive a method of enhancing photocatalytic activities [37].

Zhang *et al*. investigated the metal ions-doping on anatase TiO_2 phase and deduce that doping expands the spectrum absorption band edge and moves the absorption to the visible light region [19]. Choi *et al.* systematically studied the doping of most transitional metal elements from the periodic table of elements and analyzed the mechanism of doping using band structures [38]. It was found that the energy levels of adulterants and the conformation of the d-electrons were the important factors which affected the photo catalytic activity of TiO_2. The non-metallic ion N, carbon (C), sulfur (S) and fluorine (F) doped TiO_2 catalysts, also showed better results in enhancing the capacity to respond to

visible light [19,38]. Asahi *et al*. has studied the nitrogen doped TiO_2, whereby 0.75% of crystal lattice oxygen in the nanocrystals of TiO_2 were replaced by N and investigated its optical and catalytic properties [36]. It was shown that N doping improves catalytic effect when the catalyst is under visible light irradiation [39].

Zhang *et al.* reported the work on doping of TiO_2 with alkaline-earth metals (AEM) and illustrated that doping improves the performance of anatase TiO_2 in photocatalysis and solar cells [40]. The study used the density functional theory to investigate doping mechanisms by calculating the dopant formation energies, electronic properties, and optical properties for beryllium (Be), magnesium (Mg), calcium (Ca), strontium (Sr) and barium (Ba) doped anatase TiO_2. The calculated formation energies indicated that the substitution of Ti with an AEM atom is energetically favorable under O-rich growth conditions [40]. The electronic structure calculations suggested that, alkaline earth metals dopants shift the VBs to higher energy, and the dopant-state energies for the cases of Ca, Sr, and Ba are higher than Fermi levels, while the Be and Mg dopants result in the spin-polarized gap states near the top of VBs [40]. The components of VBs and doped-states support that the alkaline earth metals doped are active in inter-band transitions with lower energy excitations. Ca, Sr and Ba are therefore, more effective than Be and Mg in enhancing the absorbance in visible region. On the other hand, Be and Mg are superior to Ca, Sr and Ba for the absorbance improvement in near-IR region [40].

2.3 Anatase TiO_2 low index surfaces

The surface is an important component of a solid-state material, and different surfaces may exhibit different physical and chemical properties. This effect of the surface becomes especially prominent when the size of the solid is reduced to the nanoscale [41, 42]. For this reason, engineering surface structures, i.e. deliberately exposing specific facets with high energy and reactivity, has become a promising research direction in recent years and is conducted to improve the properties of the materials [43]. Much progress has been made in theoretical understanding of TiO_2 surfaces [20, 44, 45]. Increasingly powerful computational approaches have been used as is described in many recent publications [43, 46, 47]. DFT calculations have helped in understanding the structure of TiO_2 surfaces and have been a first warning sign when structure models based on experimental

observations were too simplistic (e.g. the missing-row reconstruction for the (1 1 0) surface [46] and the microfacet model for the (1 0 0) surface [47].

The surfaces of TiO_2 have played an important role in many technical applications, such as work by Fujishima and Honda that showed that photocatalytic water splitting is possible [48, 49]. Several reviews illustrate the applications of TiO_2 as a photocatalytic semiconductor [47]. Most surface science studies focus on the rutile (1 1 0) surface [47] but recently interest in anatase TiO_2 surface studies has developed [47, 50, 51]. Recently Navrotsky showed that the anatase surfaces play an important role in phase stability of TiO_2-nanoparticles [52].

Chen *et al*. investigated the important achievements on the control of specific surface structures of anatase TiO_2 crystals, focusing on facets with high surface energy [i.e. (0 0 1), (1 0 0), (1 0 1)] and their combinations using DFT calculations [53]. In addition, fascinating performances of anatase TiO_2 crystals enhanced by these high-energy surfaces were examined and discussed through the perspectives of synergistic effects of different facets and surface adsorbates, with additional insights related to some contradictory results [53]. They reported that the Fermi level of (0 0 1) facets enter their VB, while the Fermi level of (1 0 1) facets is still located at the top of the VB of (1 0 1) surface, as shown in Figure 2.4(a) [53]. When both (0 0 1) and (1 0 1) facets are exposed to the surface of anatase TiO_2 crystals, the different Fermi levels of anatase (0 0 1) and (1 0 1) facets induce the position variance of energy bands. Consequently, a so-called “surface heterojunction” could be formed between (0 0 1) and (1 0 1) on the surface of anatase TiO_2. The construction of surface heterojunction makes it possible for photogenerated electrons and holes to preferentially transfer to (1 0 1) and (0 0 1) facets, respectively, thereby leading to different reactivity on these facets as shown in Figure 2.4(b) [53]. Given the efficient spatial separation of photogenerated carriers, the co-exposure of (1 0 1) and (0 0 1) is obviously the right combination, which are beneficial for enhancing the photocatalytic performance of anatase TiO_2 crystals [53].

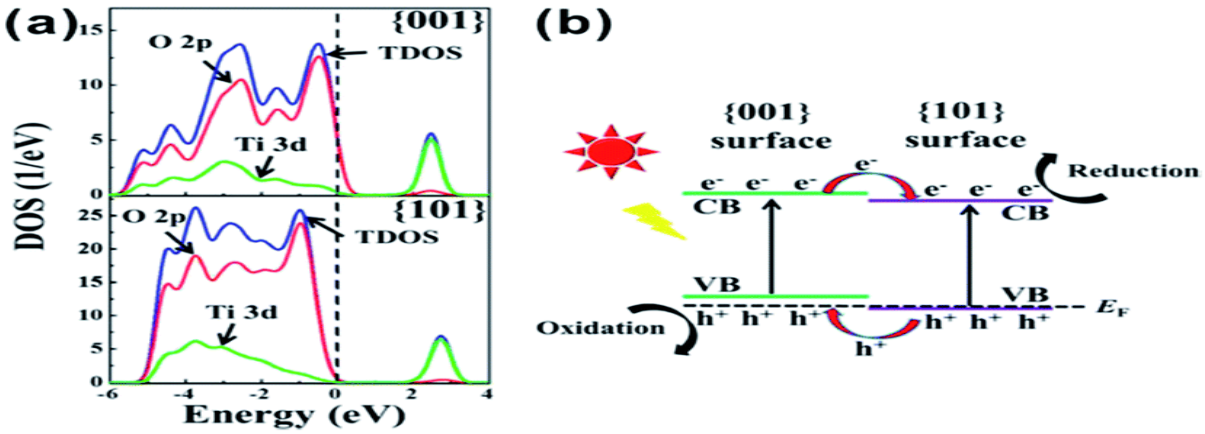

Figure 2.4 (a) Density of states (DOS) plots for (1 0 1) and (0 0 1) surface of anatase TiO_2. (b) (0 0 1) and (1 0 1) surface heterojunction [53].

Esch *et al.* investigated the surface structures and thermodynamics properties of low-index surfaces of rutile, brookite and anatase, using DFT [54]. The study compared the low-index surfaces of rutile, anatase and brookite in terms of the structural stability and relaxation. It was reported that the atomic relaxations of rutile (1 1 0), (1 0 0), anatase (1 0 1), (1 0 0) and brookite (2 1 0) surfaces, are the most common and most stable surfaces [54].

Chen *et al.* investigated the electronic structure calculations for sulfur (S) and carbon (C)-doped TiO_2 anatase (1 0 1), surfaces, using the DFT plane-wave pseudopotential method employing general gradient approximation (GGA) + U (Hubbard coefficient) functional to describe the exchange-correlation effects [45]. All the possible doping sites, including S and C dopants at lattice oxygen (O) sites (anion doping), S and C dopants at Ti sites (cation doping), and the coexisting of anion and cation doping, were investigated. Formation energies revealed that the complex of anion and cation doping configuration forms easily in the most range of O chemical potential for both S and C doping. The calculated density of states for various S and C doped systems show that the synergistic effects of S impurities at lattice O and Ti sites lead to a sharp band gap narrowing of 1.35 eV for S-doped system compared to the one of pure TiO_2 [45].

In another study, Chen *et al*. investigated N doped anatase TiO_2 (1 0 1) surface with O vacancies using the DFT plane-wave pseudopotential method [50]. The findings revealed that N doping is likely to reduce the bridging O vacancy formation energy and the cost of

substitution of O atoms with N atoms is reduced in the presence of O vacancies. The study showed that N doping has little effect on the defective surface restructuring. Their results confirmed that the mixing of N dopants-induced state with original Ti 3d and O 2p VB attributed to the band gap narrowing [50]. The reduction of the energy bandgap is 2.30 eV [50], whereas the reported theoretical value is 3.2 eV [35].

Yu *et al*. investigated the effects of electronic and local structures on the optical properties of C-doped anatase TiO_2 (1 0 1) using DFT calculation [51]. The work reported that when C is at Ti or interstitial site, a planar CO_3 unit is observed and leads to the decrease of band gap. While for C substituted at O site, although it introduces impurity states, the intrinsic band gap does not change. Furthermore, the dipole moment was calculated to explore the effect of local crystal structure on the photocatalytic ability. Furthermore, the results showed that the dipole moment can promote the separation of charge carriers and enhance the photocatalytic activity [51].

In this study, reaction mechanisms for anatase TiO_2 (1 0 0) low index surface doped with Ru and Sr are investigated using DFT, whereby electronic and optical properties are calculated. The study compares the photocatalytic activities for undoped and Ru- and Sr-doped systems using substitutional and adsorption mechanisms.

Chapter 3

3. Methodology

3.1 Density Functional Theory

DFT is an extremely successful approach for the description of the ground state properties of metals, semiconductor and insulators. It is based on the remarkable theorems by Hohenberg and Kohn [55] who demonstrated that the total energy of a many-electron system in an external potential is a unique functional of the electron density for a given position of atom nuclei. The Hohenberg Kohn theorems stated as following:

Theorem 1: State that the ground state of a many-electron system (under the effects of an external potential) is uniquely defined by the ground state electron density [55].

Theorem 2: State that the existence of an energy functional of the density $E[n]$ that is minimal for the ground state density $n_0(r)$ giving the ground state energy [55].

The proof is given for a non-degenerate ground-state but may easily be expanded to degenerate ground state as well. Let $n(r)$ be the non-degenerate density of N electrons in the potential $v_1(r)$, corresponding to the ground state Phi_1 and the energy E_1. Then:

$$E_1 = \langle \Phi_1 | H_1 \Phi_1 \rangle = \int v_1(r) n(r) dr + \langle \Phi_1 | (T+U) \Phi_1 \rangle \quad (1)$$

where H_1 is the total Hamiltonian corresponding to v_1 and *T* and *U* are the kinetic and interaction energy operators. Now assume that there exists a second potential $v_2(r)$, not equal to $v_1(r)$ +constant, with ground state Φ_2, necessarily ≠ $e^{i\Theta}\Phi_1$, which gives rise to the same $n(r)$. Then

$$E_2 = \int v_2(r)\, n(r) dr + \langle \Phi_2 | (T+U) \Phi_2 \rangle \quad (2)$$

since Φ_1 is assumed to be non-degenerate, the variational principle for Φ_1 gives rise to the following inequality:

$$E_1 < \langle \Phi_2 | H_1 \Phi_2 \rangle = \int v_1(r) n(r) dr + \langle \Phi_2 | (T+U) \Phi_2 \rangle \quad (3)$$

$$= E_2 + \int [v_1(r) - v_2(r)] n(r) dr$$

analogously

$$E_2 \leq \langle \Phi_1 | H_2 \Phi_1 \rangle = E_1 + \int [v_2(r) - v_1(r)] n(r) dr \quad (4)$$

where ≤ is used since non-degeneracy of Φ_2 was not assumed. Adding equations (3) and (4) leads to contradiction:

$$E_1 + E_2 < E_1 + E_2 \tag{5}$$

This shows that the assumption of the second potential $v_2(r)$, which is unequal to $v_1(r)$ + constant but yet yields the same $n(r)$. Since $n(r)$ determines both N and $v(r)$ it gives us the full H and N for the electronic system. Therefore $n(r)$ implicitly determines all properties of the system derivable from the Schrödinger equation for H.

The minimum value of the total energy functional is the ground state energy of the system, and the density that yields this minimum value is the exact ground state density. The electron density is a scalar function defined at each point r in real space, $\rho = \rho(r)$. In DFT, the total energy is expressed by [55, 56]:

$$E = E\left[\rho(\mathrm{r}), \mathrm{R}_\alpha\right] \tag{6}$$

where the electron density ρ and total energy E depends on the type and arrangement of the atomic nuclei; R_α denotes the positions of the nuclei α in the system. This equation is the key to the atomic-scale understanding of structural, electronic and magnetic properties of matter. While the Hohenberg-Kohn theorem shows that it is possible to use the ground state density to calculate properties of the system, it does not provide a way of finding the ground state. A route to this is provided by the Kohn-Sham equations [57]. The kinetic and interaction energy were treated by reintroducing Kohn-Sham approach of a special type of wavefunctions (single particle orbitals) into the formalism. The Kohn-Sham DFT is a widely used and successful method for electronic structure calculations. The accuracy of DFT calculations depends on the choice of approximation of the universal exchange correlation (XC) functionals. In Kohn-Sham DFT, the total energy of a system is expressed as a functional of the charge density by [55]:

$$E[\rho] = T_s[\rho] + \int dr\, V_{ext}(r)\rho(r) + E_H[\rho] + E_{xc}[\rho] \tag{7}$$

where T_S is the sum of the kinetic energies of all effective electrons moving as independent particles. In DFT the real electrons of a system are replaced by effective electrons with the same charge, mass and density distribution. However, effective electrons move as independent particles in an effective potential, whereas the motion of a real electron is correlated with those of all electrons. If each effective electron is described by a single particle wave function ϕ_i, then the kinetic energy of all effective electrons in the system is given by [55, 57]:

$$T_s[\rho] = \sum_{i=1}^{N} \int dr \phi_i^*(r) \left(-\frac{\hbar^2}{2m} \nabla^2 \right) \phi_i(r) \tag{8}$$

V_{ext} is the external potential acting on the interacting system (at minimum, for a molecular system, the electron-nuclei interaction), E_H is the Hartree (or Coulomb) energy and can be expressed by [55, 57]:

$$E_H = \frac{e^2}{2} \int dr \int dr' \frac{\rho(r)\rho(r')}{|r - r'|} \tag{9}$$

and E_{XC} is the exchange-correlation energy per particle of a homogeneous electron gas of charge density ρ. The Kohn–Sham equations are found by varying the total energy expression with respect to a set of orbitals to yield the Kohn–Sham potential by [55]:

$$V_{eff}(r) = V_{ext}(r) + e^2 \int \frac{\rho(r')}{|r - r'|} dr' + \frac{\delta E_{xc}[\rho]}{\delta \rho(r)} \tag{10}$$

where the last term described by:

$$v_{xc}(r) \equiv \frac{\delta E_{xc}[\rho]}{\delta \rho(r)}$$

and is called the exchange-correlation potential. The sum of the orbital energies is related to the total energy as [55]:

$$E = \sum_{i}^{N} \varepsilon_i - V_H[\rho] + E_{xc}[p] - \int \frac{\delta E_{xc}[\rho]}{\delta \rho(r)} \rho(r) dr \quad (11)$$

This equation only holds true for specific choices of orbital energies [55, 56, 57]:

The schematic of self-consistent field (SCF) cycles are continued till convergence is reached, for example when the total energy of two successive iterations deviates from each other by less than a convergence criterion ε (for example, 0.001 Ry). At this stage one can look at forces acting on the atoms in the unit cell. If symmetry allows there can be forces on the atoms which are defined as the negative gradient of the total energy with respect to the position parameters. Figure 3.1 represent the flow chart of electronic structure methods used for solving Kohn-Sham equations [55, 56, 57, 58]:

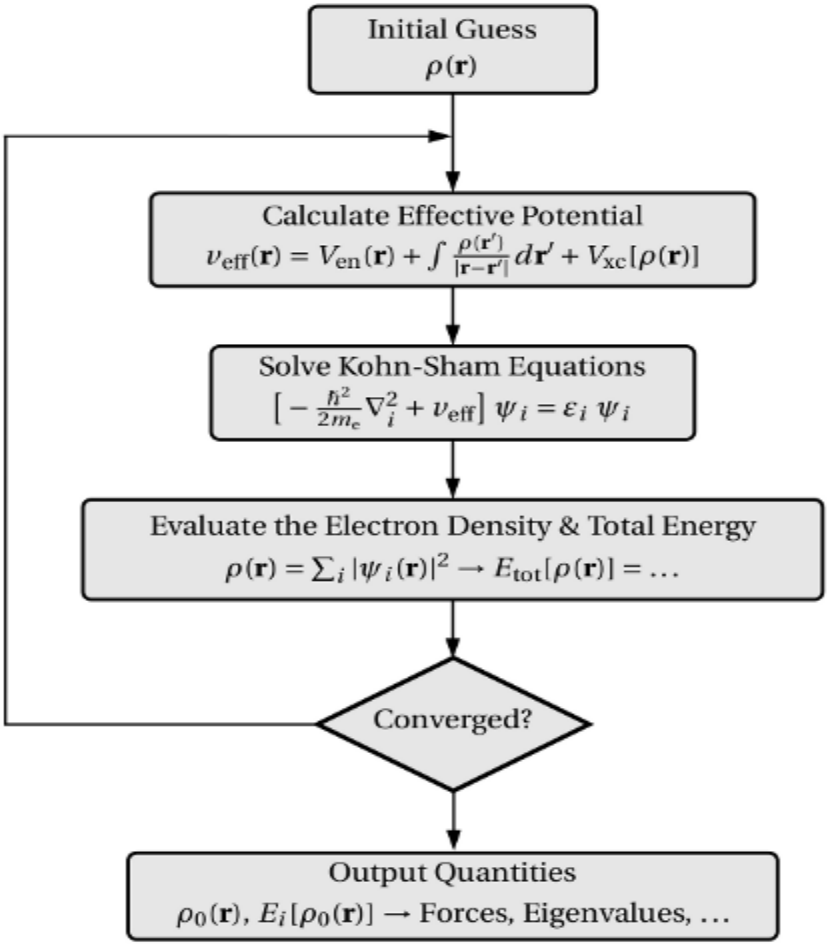

Figure 3.1 Flow chart of electronic structure methods used for solving Kohn-Sham equations [59].

As shown in the flow chart of the iteration scheme, the initial guess for the electron density, which is required for the calculation of $v_{eff}(r)$. The diagonalization of the Kohn-Sham equations, and the subsequent evaluation of $\rho(r)$ along with E_{tot} is then done as a second step. As long as the convergence criterion is not fulfilled, the numerical procedure is continued with the last $\rho(r)$ instead of the initial guess. When the criterion is satisfied, various output quantities are computed.

3.1.1 Local Density Approximation

Local-density approximations (LDA) are a class of approximations to the exchange–correlation energy functional in DFT that depends solely upon the value of the electronic density at each point in space (and not, for example, derivatives of the density or the Kohn–Sham orbitals). The exchange-correlation energy equation of LDA is given as [60, 61, 62]:

$$E_{xc}^{LDA}[\rho] = \int \rho(r)\varepsilon_{xc}(\rho)\,\mathrm{dr} \tag{12}$$

where ρ is the electronic density and ε_{xc} is the exchange-correlation energy per particle of a homogeneous electron gas of charge density. The exchange correlation energy is decomposed into exchange and correlation terms linearly and can be expressed as [60-63]:

$$E_{xc} = E_x + E_c \tag{13}$$

so that separate expressions for E_x and E_c are sought.

Despite the remarkable success of the LDA, it has also limitations. For systems where the density varies slowly, the LDA tends to perform well, and chemical trends are well reproduced. In strong correlated systems were independent particle picture breaks down, the LDA is very inaccurate. For example, the LDA has been applied to high T_c superconductors, but finds several to be metallic, when they are insulating at 0K [64]. LDA finds, the wrong ground states in many simpler cases by underestimating bondlengths and lattice constants by roughly 10% [65]. In LDA the weak bonds are too short and the calculated binding energies are typically too large [66]. An improvement to

this can be made by considering the gradient of the electron density, the so called generalized gradient approximation (GGA).

3.1.2 Generalized Gradient Approximation

As the LDA approximates the energy of the true density by the energy of a local constant density, it fails in situations where the density undergoes rapid changes such as in molecules. An improvement to this can be made by considering the gradient of the electron density, the so-called GGA. Beyond the LDA the exchange and correlation in an inhomogeneous system is non-local with respect to electrons it surrounds, and this is referred to as gradient correction or GGA, which was introduced by Perdew and Wang [63]. The GGA exchange correlation energy is written as [67]:

$$E_x{}^{GGA}c(n) = \int drn(r)\varepsilon_{xc}^{GGA}\left[n(r), \| \nabla n(r) \|\right] \tag{14}$$

where ε_{xc} is the exchange correlation energy and $n(r)$ is the gradient term. The GGA has been widely used and proved to be quite successful in correcting some of the deficiencies of the LDA, and in correcting the magnetic ground. GGA was found to overestimate bondlenghts and lattice constants.

3.2 Plane-wave pseudopotential method

The plane-wave pseudopotential method has become a powerful and reliable tool to study the properties of a broad class of materials. The emphasis on the total energy and the related properties makes plane-wave pseudopotential a technique suited to structural studies based on a quantum-mechanical treatment of the electronic subsystem [67]. The main idea of the method is to simplify the DFT problem by considering only valence electrons. Core electrons are excluded under the assumption that their charge density is not affected by the changes in the chemical environment. This approximation is well understood and gives several computational advantages such that [67, 68, 70]:

(i.) The pseudopotential is much weaker in the core region than the true Coulomb potential of the nucleus and it does not have a singularity at the position of the nucleus.

(ii.) The resulting pseudo-wave functions are smooth and nodeless in the core region.

(iii.) There are fewer electronic states in the solid-state calculation.

(iv.) Both pseudopotentials and pseudo-wave functions can be efficiently represented using a plane wave basis set. The plane-wave pseudopotential method is applicable to large systems that are subject to 3D periodic boundary conditions [67-69].

3.2.1 Plane-wave basis

An infinite plane-wave basis set is used to expand the electronic wave functions of the system. The method is described well by using Bloch's theorem, which state that the electronic wave function at each k-point can be expanded in terms of a discrete plane-wave basis set i.e. [70-72]:

$$\Psi_{ki}(r) = exp[ik.r]\, f_i(r) \tag{15}$$

This expression has a wavelike and cell-periodic part. The function $f_i(r)$ defines the periodicity of the solid and can be expanded using a basis set with a discrete set of plane waves, written as [71, 72]:

$$f_i(r) = \sum_G G_{i,G} exp[iG.r] \tag{16}$$

where the G_i are the reciprocal lattice vectors of the periodic cell. Thus, each electronic wave function can be written as a sum of plane waves,

$$\Psi_{ki}(r) = \sum_G G_{i,k+G}\left[i(\mathrm{k}+G).\mathrm{r}\right] \tag{17}$$

where $G_{i,K+G}$ are the coefficients for the plane waves that need to be solved and depend entirely on the specific kinetic energy, $\left(\frac{h^2}{2m}\right)|K+G|^2$.

The convergence of this expansion is controlled by the choice of the kinetic energy cutoff. In practice, the plane wave basis set is limited by including all plane waves whose kinetic energies are less than some cutoff energy E_{cut}. Introduction of an energy cut-off to the

discrete plane-wave basis set produces a finite basis set. The truncation of the plane-wave basis set at finite cut-off energy will lead to an error in the computed total energy. However, it is possible to reduce the magnitude of the error by increasing the value of the cut-off energy. In principle, the cut-off energy should be increased until the calculated total energy has converged.

The plane-waves are used as a basis set for the electronic wave functions, and substitution of equation (15) into equation (11) and the integration over r gives the following secular equation:

$$\sum_{G'}\left[\frac{h^2}{2m}|k+G|^2\,\delta_{GG'}+V_{ion}(\mathrm{G}-\mathrm{G}')+V_H(\mathrm{G}-\mathrm{G}')\right]C_{i,k+G'}=\varepsilon_i C_{i,k+G} \tag{18}$$

The first contribution, the kinetic energy, is diagonal, whereas the various potential contributions are given by their Fourier transforms. This may be written in terms of the Hamiltonian matrix elements $H_{K+G,K+G}$ as:

$$\sum_{G'}H_{k+G,K+G'}C_{i,k+G'}=\varepsilon_i C_{i,k+G'}. \tag{19}$$

The solutions of the Kohn-Sham equation are obtained by diagonalizing the Hamiltonian matrix elements $H_{K+G,K+G}$. The size of these matrix elements is determined by the choice of energy cut-off $\left(\frac{h^2}{2m}\right)|K+G|^2$,and will be large for systems that contain both valence and core electrons.

Although Bloch's theorem states that the electronic wave functions can be expanded using a discrete set of plane-waves, a plane-wave basis set is usually very poorly suited to expanding electronic wave functions because a very large number of plane- waves are needed to expand the tightly bound core orbitals and to follow the rapid oscillation of the wave functions of the valence electrons in the core region [70]. An extremely large plane-wave basis set would be required to perform all-electron calculation, and a vast amount of computational time would be required to calculate the electronic wave functions. This problem can be overcome using pseudopotential approximation [73,74].

3.2.2 The pseudopotential method

The physical properties of solids are dependent on the valence electrons to a much great extent than on the core electrons. In the pseudopotential method, the core electrons and the strong attractive Coulomb potential inside the ionic core are replaced by a weaker pseudopotential that describes all the salient features of a valence electron moving through a crystal, including relativistic effects [75, 76]. Thus, the original solid is now replaced by pseudo valence electron and pseudo-ion cores. These pseudoelectrons experience the same potential outside the core region as the original electrons but have a much weaker potential inside the core region. Figure 3.3 illustrates the ionic potential (V_{AE}), the valence wave function (Ψ_v), the corresponding pseudopotential (V_{pseudo}) and pseudo-wave function (Ψ_{pseudo}) respectively [77].

The valence wave functions oscillate rapidly in the region occupied by the core electrons due to the strong ionic potential in this region. The oscillations maintain the orthogonality between the core and valence wave functions, which is required by the exclusion principle. The pseudopotential is constructed ideally, so that its scattering properties or phase shifts for the pseudo wave functions are identical to the scattering properties of the ion and the core electrons for the valence wave functions, but in such a way that the pseudo wave functions have no radial nodes in the core region. In the core region, the total phase shift produced by the ion and the core electrons will be greater by π, for each node that the valence functions had in the core region, than the phase shift produced by the ion and the valence electrons. Outside the core region the two potentials are identical, and the scattering from the two potential is indistinguishable.

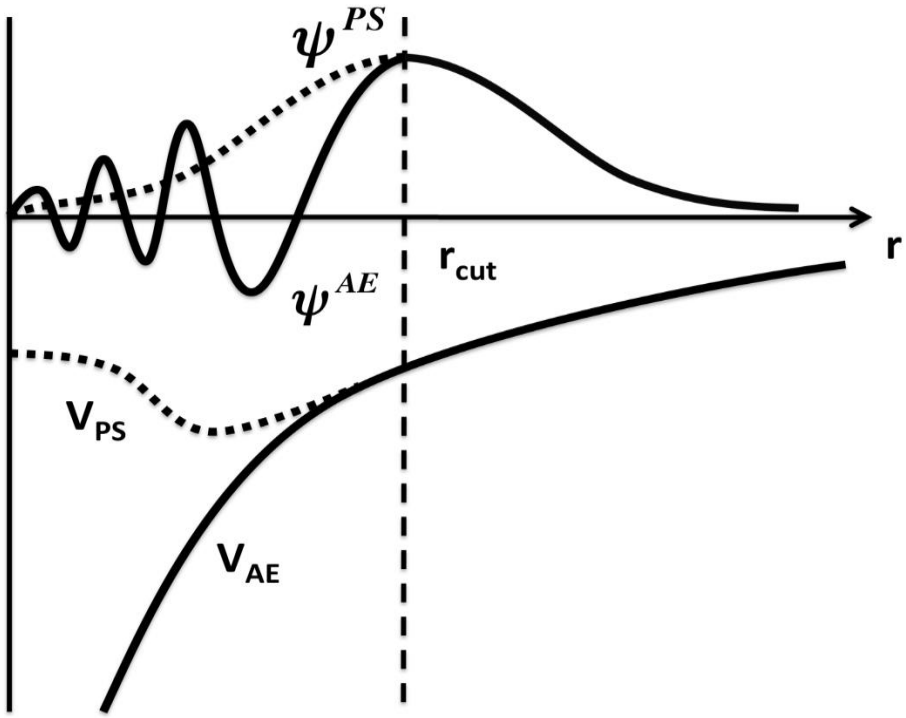

Figure 3.2 Schematic of the smoothing effect of the pseudo-wavefunction (Ψ_{pseudo}) and potential (V_{pseudo}) compared to the all-electron (AE) versions [78].

The advantage of using the pseudopotential approximation is that it allows the electronic wave function to be expanded using a much smaller number of plane-wave basis states, so that a smaller amount of computational time would be required for convergence of the energies. The pseudopotential has the form

$$V_{NL} = \sum_{lm} |lm\rangle V_l \langle lm|, \tag{20}$$

where $|lm\rangle$ is the spherical harmonics and V_l is the pseudopotential for angular momentum l. Most the pseudopotential currently used in the electronic structure is generated from all electron atomic calculations.

A pseudopotential that uses the same potential for all the angular momentum components of the wave function is called a local pseudopotential. A local pseudopotential is a function that only depends on the distance dependence of the potential. The norm-conserving pseudopotential (NCP) by Kleinmann and Bylander [79] is an example of a non-local

pseudopotential, using a different potential for each angular momentum component of the wave function.

Recently, the ultrasoft pseudopotential (USP) put forward by Vanderbilt has been implemented in plane-wave calculations. In this scheme the pseudo-wave-functions can be as soft as possible within the core region. They cover a wide range of atoms, including the transition metals. It allows for an efficient representation of single-particle wave functions in the vicinity of the atomic cores where they can vary rapidly. In this study, we use the ultrasoft pseudopotential by Vanderbilt [80] within the CASTEP program [81] for total energy calculations since they give accurate results for the systems under investigation.

3.2.3 Brillouin zone sampling

Many calculations in crystals involve the averaging over the Brillouin zone [82], of periodic functions of wave vector. Such calculations are long, complicated and in principle require knowledge of the value of the function at each k-point in the Brillouin zone. Electronic states are allowed only at a set of k-points determined by the boundary conditions that apply to bulk solid. Due to the Bloch theorem [70], the infinite number of electrons in the solid is accounted for by an infinite number of k-points and only a finite number of electronic states are occupied at each k-point. The occupied state at each k-point contributes to the electronic potential in the bulk solid so that, in principle, an infinite number of calculations are needed to compute this potential. All required function of k-point, the potential is continuous so the integral over the infinite number of k-points can be replaced by a sum over a finite, often small number.

DFT approximate the k-space integral with a finite sampling of k-points. Special k-points scheme have been developed to use the fewest possible k-points for a given accuracy, thereby reducing the computational cost. The most commonly used scheme is that of Monkhorst and Pack [83]. Monkhorst and Pack (MP) proposed a scheme where k is distributed homogeneously in the Brillouin zone per:

$$\vec{k} = x_1\vec{b_1} + x_2\vec{b_2} + x_3\vec{b_3} \tag{21}$$

where $\vec{b}_{1\ldots3}$ the three-reciprocal basis are vectors and $x_{1\ldots3}$ are the supplied values.

$$X_i = \frac{1}{n_i} \tag{22}$$

Where $i = 1, \ldots, n_i$ where n_i are the folding parameters. MP scheme essentially means that the sampling k-points are distributed homogeneously in the Brillouin zone, with rows or columns of k-points running parallel to the reciprocal lattice vectors that span the Brillouin zone.

The number of k-points necessary for a calculation depends entirely on the system as the treatment of metals, semiconductors and insulators is different. Metallic systems require an order of magnitude more k-points than semiconductor and insulating systems and dense k-space meshes to define the Fermi surface precisely. If the k-points sampling does not give a well converged total energy, then a much denser set of k-points must be used to reduce the errors and ensure the required convergence. Therefore, choosing a sufficiently dense mesh of summation is crucial for the convergence of the results, and is therefore one of the major objectives when performing convergence tests.

3.2.4 Convergence tests

The tag k-spacing determines the number of k-points, if the k-points file is not presented. The file k-points must contain the k-point coordinates and weights or the mesh size for creating the k-point grid. Since k spacing is the smallest allowed spacing between k-points in units of $Å^{-1}$. The number of k-points increases when the spacing is decreased. In the reciprocal mode, the k-points are given by equation (16). But in the Cartesian input format the k-points are given by:

$$\vec{k} = \frac{2\pi}{a}(x_1, x_2, x_3) \tag{23}$$

The following example illustrates how to specify the k-points. The unit cell of an FCC lattice is spanned by the following basis vectors:

$$A = \begin{pmatrix} 0 & a/2 & a/2 \\ a/2 & 0 & a/2 \\ a/2 & a/2 & 0 \end{pmatrix} \tag{24}$$

The reciprocal lattice is defined as

$$2\pi B = \begin{pmatrix} -1 & -1 & 1 \\ 1 & -1 & 1 \\ 1 & 1 & -1 \end{pmatrix} \quad (25)$$

The importance of testing energy cut-off and k-points is to get the good convergence of the total energy; however, the number of k-points depend on the system. In this study, we used the Monkhorst and Pack to determine the energy cut-off. Thereafter, the determined energy cut-off was used to determine the suitable k-points for bulk anatase TiO_2.

3.3 Computer code

3.3.1 Cambridge Serial Total Energy Package

Cambridge Serial Total Energy Package (CASTEP) is a state-of-the-art quantum mechanics-based program designed specifically for solid state materials science (that is, crystals and surfaces in materials such as semiconductors, ceramics, metals, minerals, and zeolites) [79, 82]. It employs the DFT plane-wave pseudopotential method, which allows the performance of first-principles quantum mechanics calculations. Using CASTEP, calculations can be performed using exchange-correlation (XC) local and semi-local functions approximations of the LDA and GGA approximations [82]. The CASTEP code was used to perform all the calculations presented in this study.

3.3.2 Computational details

The first-principles calculations were performed using the CASTEP code in materials studio developed by Accelrys Software Inc [79]. The energy plane-wave pseudopotential total energy calculation method based on DFT was used to carry out all the calculations. For structural optimization, GGA with the Perdew-Burke Ernzerhof (PBE) exchange-correlation functional was employed for all the calculations to obtain the electronic structures and optical properties. In these calculations, the energy cut-off for the plane-wave basis was set to be 600 eV and the Brillouin zone was represented by a Monkhorst-Pack (MP) scheme for the generation of k-points of 7 x 7 x 3.

The convergence threshold for self-consistent tolerance was set to $2.0e^{-6}$ eV/atom and geometric relaxation was obtained with the Broyden-Fletcher-Goldfarb-Shanno (BFGS) algorithm until the atomic relaxations were below 0.05 eV/Å. The above-mentioned

parameters were suitable for getting well-converged total energy and geometry optimization results. In the geometry optimization, the convergence criteria for structural optimization were set to be medium quality with the energy change, maximum stress and maximum displacement of $2.0e^{-5}$ eV/atom, 0.1 GPa and 0.002 Å, respectively. For optical properties calculations, polycrystalline models and scissors operators were adapted.

CHAPTER 4

4. Results and discussions

In this chapter the results obtained from quantum-mechanical calculations defined in chapter 3 are presented. The results present the computational study of electronic and optical properties of undoped and anatase TiO_2 (1 0 0) surface doped with Ru and Sr. The following three doping mechanism were considered, namely:

(i) adsorption of a dopant on the top layer of the surface
(ii) adsorption of a dopant inside the layers of the surface
(iii) replacement of one Ti atom with dopant atom.

All the calculations were performed using the plane wave pseudopotential method as implemented in the CASTEP code.

4.1 Convergence test for bulk anatase TiO_2

Convergence tests are methods of testing where power series make sense (. i.e. conditional convergence, absolute convergence, energy convergence and interval of convergence). In this study, we optimized the bulk structure of anatase TiO_2 to reach optimal condition using the converged energy cut-off and k-points. Figure 4.1 and 4.2 illustrate a way of finding the converged energy cut-off and k-points.

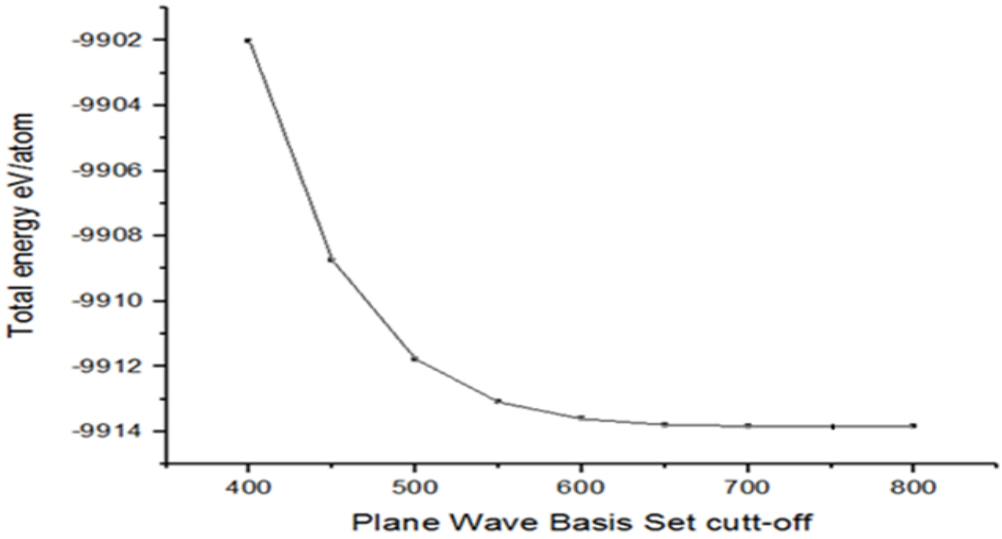

Figure 4.1 Total energy as a function vs kinetic energy cut-off for anatase TiO_2.

The graph of total energy versus kinetic energy cut-off for TiO_2 anatase bulk structure is shown in Figure 4.1. It was observed that from 600 eV the total energy is independent of energy cut-off suggesting that the energy has converged. The energy difference between 600 eV and 650 eV is 50 eV. To find converged k-points, the well- converged kinetic energy cut-off was used for farther calculations.

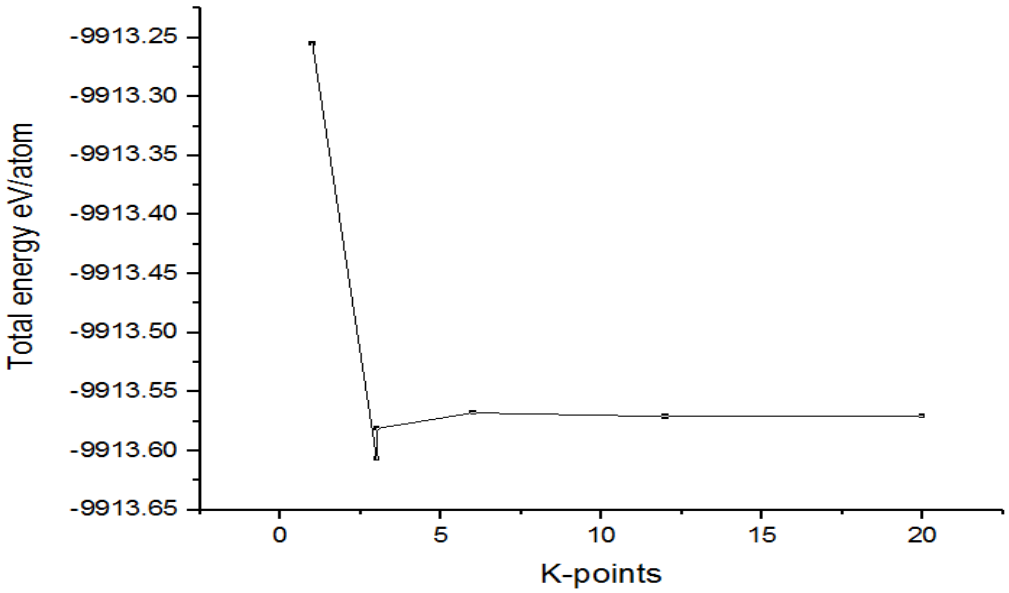

Figure 4.2 Total energy as a function of number of k-points of anatase TiO_2.

The graph of total energy versus number of k-points is shown in Figure 4.2. The total energies of the system as a function of k-points were calculated. From Figure 4.2 the graph becomes more stable at the total energy of -9913.570 eV which corresponds to the 7 x 7 x 3 monkhorst pack mesh k-points parameters. The corresponding k-points were considered as the most preferred mesh. All the geometry optimization calculations in this study were performed using 600 eV energy cut-offs and 7×7×3 k-points to find electronic and optical properties of bulk, undoped and Ru and Sr-doped surfaces of anatase TiO_2.

4.2 Bulk anatase TiO_2

4.2.1 Structural properties

After full structural optimization, the lattice parameters for bulk anatase TiO_2 are found to be a = 3.800 Å, c = 9.720 Å for the anatase phase as shown in Table 4.1. The results

obtained are in good agreement with the known experimental data and previous theoretical results [20, 80, 84, 85, 86].

Table 4.1. The optimized structural parameters of bulk anataseTiO_2.

Parameters	Experimental [80]	This work	Literature [20, 84, 85,86]
a (Å)	3.780	3.801	3.781
c (Å)	9.501	9.720	9.510
deq (Å)	1.932	1.950	1951
dap (Å)	1.980	2.000	2.000
c/a (Å)	2.510	2.558	5.510

Table 4.1 illustrates the known experimental, previous theoretical and current work of the structural parameters of bulk anatase TiO_2, which are a=b, c, d ($_{deq}$ and $_{dap}$ are the equatorial and apical Ti–O bond lengths, respectively) and c/a. The comparisons between the structural parameters obtained in this work and experimental data, deviated by 0.02% along a=b-axis and 0.22% along the c-axis, while the previous theoretical results reported in [81] gave deviations of 0.02% along a=b-axis and 0.23% along the c-axis. The calculated percentage errors are within a reasonable and acceptable value as determined by various methods and codes [20, 84, 85, 86].

4.2.2 Electronic properties

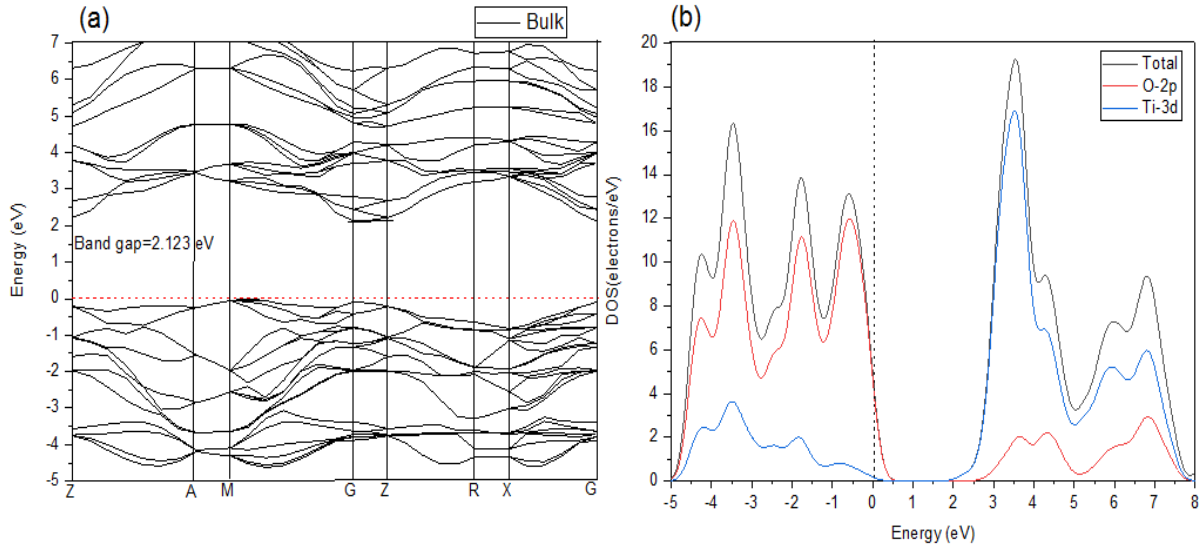

Figure 4.3 (a) The K-points band structure and (b) density of states of anatase TiO_2 bulk structure.

In order to conveniently investigate the electronic structure of bulk anatase TiO_2 the k-points obtained in Figure 4.2 were used. Figure 4.3 shows the band structure of bulk anatase TiO_2 and it is observed that the band gap is about 2.123 eV. This is less than the experimental result of 3.230 eV. It is well known that the underestimated energy band gap can be due to the choice of exchange-correlation energy. The scissor operation of 1.107 eV was then employed for both undoped and doped anatase TiO_2 (1 0 0) surface to compensate for the underestimation of the energy band gap. The top of valence band (VB) approximately locates near the M-point and the bottom of the conduction band (CB) locates at the G-point, which means that TiO_2 with anatase structure is an indirect-gap material. The VB shifts to near the Fermi levels, which means that anatase TiO_2 is a p-type semiconductor. The VB of bulk TiO_2 mainly consists of the 2p, 2s states of O and 3d states of Ti. In the uppermost VB, the O-2p states are predominantly found between -5 and 0 eV. The Ti 3d states give rise to some bands in the energy range from -5 to -3 eV. The lowest conduction band is dominated by Ti-3d states. Meanwhile, the hybridization between the Ti-3d and O-2p levels at the VB is observed.

Density of states (DOS) describes the number of available states per distance of energy at each energy state which can be occupied by electrons [82]. A great DOS (highest peak) at a given energy state means that there are numerous available states to be occupied by electrons, while a DOS of zero represents no state that to be occupied by electrons. The total density of states (TDOS) and partial density of states (PDOS) graphs of bulk anatase TiO_2 are presented in Figure 4.3 (b). By combining TDOS and PDOS, three features can be summarized: from the graph in the range of -5.00 eV to 8.00 eV, there are two regions, VB at around -5.00 eV to 0.50 eV and CB at around 2.00 eV to 8.00 eV. The VB and CB mainly consist of O-2p and Ti-3d states, respectively, while CB is decomposed into $Ti_{eg(>8eV)}$ and $t_{2g(<8eV)}$. The band width of the VB is 5.50 eV.

4.2.3 Optical properties

The optical properties for dielectric function, refractive index, reflectivity, absorption coefficient and loss function derived from the effect of light passing through the optimized bulk anatase TiO_2 are analyzed. These optical properties are related to the complex dielectric function by the following relation [87]:

$$\xi(\omega) = \xi_1(\omega) + \iota\xi_2(\omega) \tag{26}$$

where $\xi(\omega)$ is real part and $\xi_2(\omega)$ is an imaginary part. The real part is associated with the electronic polarizability of the material while the imaginary part is correlated to the electronic absorption of the material. The imaginary part of dielectric function can be defined as [87]:

$$\varepsilon_{2(\hbar\omega)} = \frac{2\pi e^2}{\Omega\varepsilon_0}\sum_{k,v,c}\left|\Psi_k^c\right|u.r\left|\Psi_k^v\right|^2\delta\left(E_k^c - E_k^v - E\right) \tag{27}$$

where $e, u.\Psi_k^v$ and Ψ_k^c represents electronic charge, incident electric field, VB and CB wave function at k-point, respectively. The Kramers-Kroning relation is used to obtain the

real part of dielectric function from the imaginary part. The relation of refractive index n(w), and extinction coefficient k(w) with real part are as follows [87]:

$$n(\omega) = \sqrt{\frac{|\varepsilon(\omega)| + \varepsilon_1(\omega)}{2}} \quad (28)$$

$$k(\omega) = \sqrt{\frac{|\varepsilon(\omega)| - \varepsilon_1(\omega)}{2}} \quad (29)$$

All the optical properties of bulk anatase TiO_2 were calculated from the standard DFT calculation (see Figure 4.4 to 4.6).

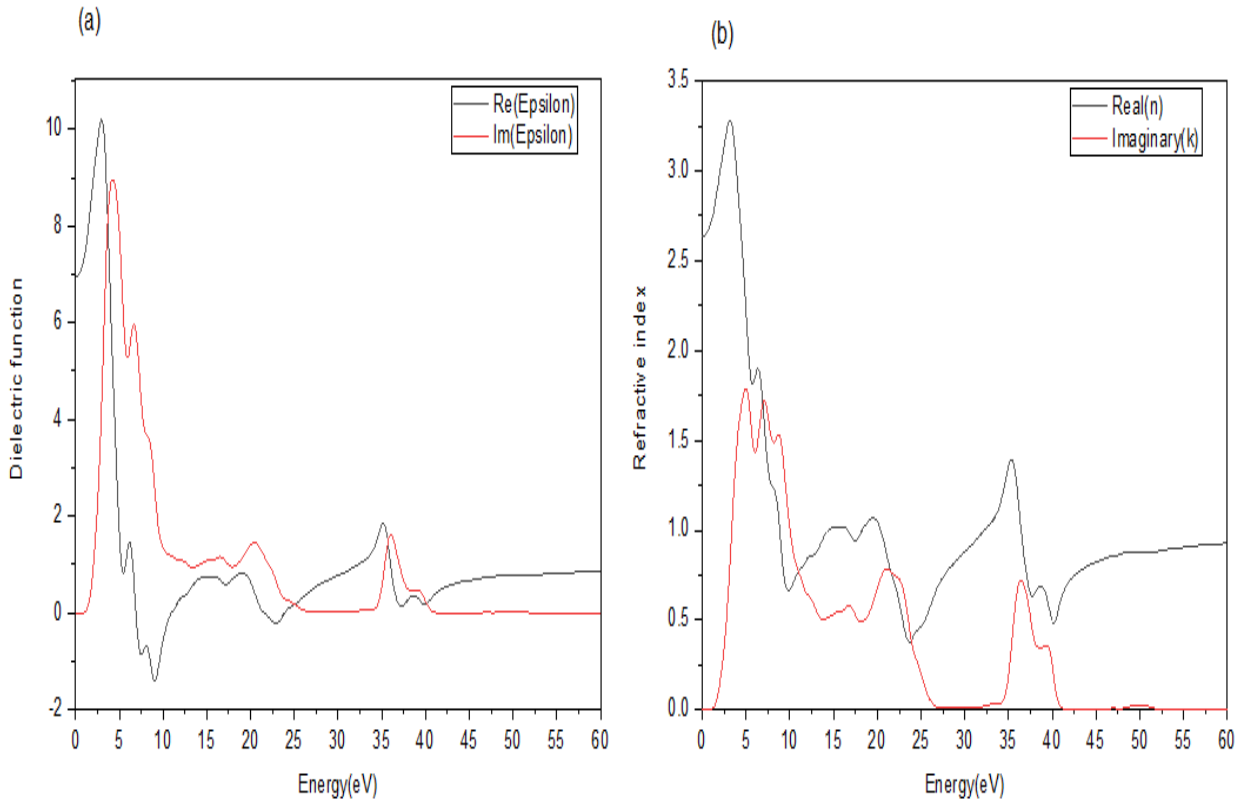

Figure 4.4 Calculated (a) real and imaginary parts of dielectric function and (b) refractive index and extinction coefficient.

Figure 4.4 illustrates the bulk anatase TiO_2 dielectric function and refractivity index up to a photon energy of 60 eV, where the black and red lines represent the real and imaginary

parts respectively. The dielectric constant from the standard functional presented the value of 5.30 eV as illustrated in Figure 4.4. The real part of the dielectric function shows the highest peak intensity at 4.90 eV. The imaginary part shows the first energy peak at about 3.08 eV. These peaks belong to the electronic transition from O- 2*p* to Ti-3*d* states at the VB and CB respectively. The computed highest peak of real part refractive index is at 2.50 eV as illustrated in Figure 4.4. The extinction coefficient is the imaginary part of the refractive index, which can be related to the light absorption. The major peak of extinction coefficient is at 4.19 eV. The high dielectric constant and refractive index of anatase TiO_2 make it a suitable possible candidate for efficient light harvesting efficiency.

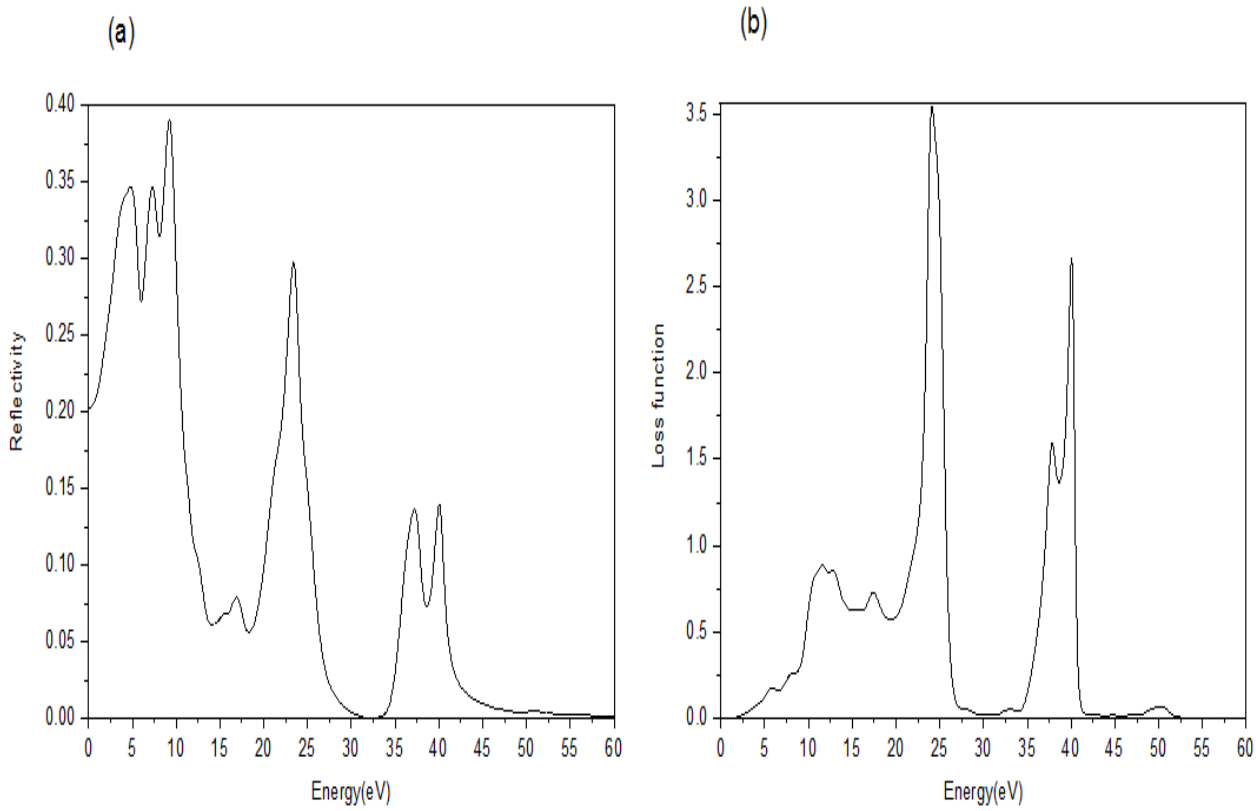

Figure 4.5 (a) Reflectivity and (b) loss function of bulk anatase TiO_2.

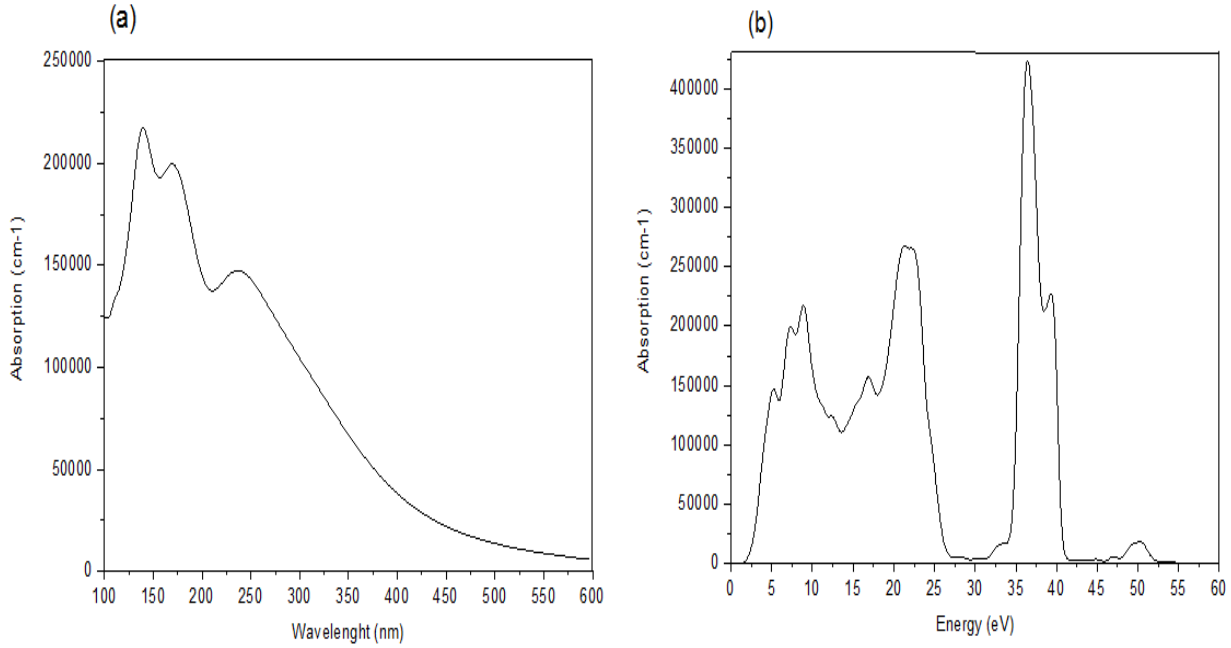

Figure 4.6 (a) The absorption coefficient of bulk anatase TiO_2 against wavelength and (b) photon energy.

Figure 4.5 to 4.6 represented bulk anatase TiO_2 reflectivity and loss function, and absorption coefficients respectively. These optical properties can be related to the dielectric function through the following relation:

$$R(\omega)=\frac{(n-1)^2+k^2}{(n+1)^2+k^2} \tag{30}$$

$$L(\omega)=\mathrm{Im}\left(\frac{-1}{\varepsilon(\omega)}\right)=\frac{\varepsilon_2(w)}{\varepsilon_1^2(\omega)+\varepsilon_2^2(\omega)} \tag{31}$$

$$\alpha(\omega)=\frac{2k\omega}{c} \tag{32}$$

The major peaks of the reflection spectra from reflectivity occurred at 10.97 eV as shown in Figure 4.5 and can be seen to occur where the peak of dielectric function and refractive index start decreasing and reaching zero (see Figure 4.4 and 4.5). The loss function is

energy loss of electrons when passing through uniform dielectric material. The major peak of energy loss function is positioned at 23.50 eV that match to the sharp decline in the reflection spectra in Figure 4.5. The absorption coefficient determines how far light of a particular wavelength can penetrate into a material before it is absorbed. The energy and wavelength of absorption can be defined by difference between energy levels of an electronic transition. The optical absorption of bulk anatase TiO_2 occur in the UV light region at an absorption edge from 300 to 400 nm as shown in Figure 4.6. The prominent peak intensity for absorption values of anatase is $4.77x10^5$ corresponding to the energy highest peak at 36.5 eV. The energy peak of the absorption spectrum can be observed to display in the same peaks of reflection and loss function spectrum.

4.3 Anatase TiO_2 (1 0 0) surface

In this study, the (1 0 0) low index surface structure of anatase TiO_2 was created and modeled by cleaving the optimized bulk structure and then build a slap for surface as shown in Figure 4.7. After the surface was built, it was then optimized to get an optimal ground state structure.

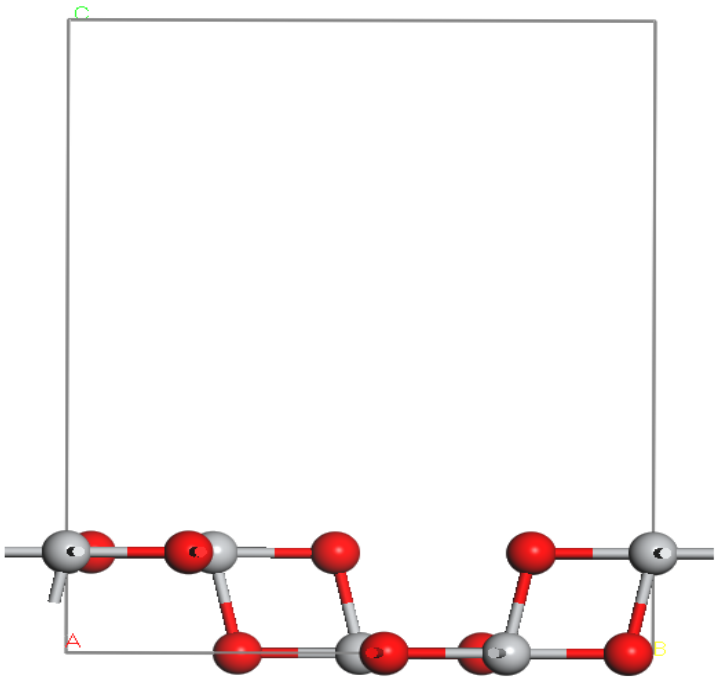

Figure 4.7 Cleaved (1 0 0) low index surface from anatase TiO_2.

4.3.1 Ru and Sr-doped anatase TiO_2 (1 0 0) surface

After the cleaved surface was optimized, doping effects were examined using two approaches, substitutional and adsorption mechanisms. In the case of substitutional mechanism, one Ti from TiO_2 (1 0 0) surface was replaced by dopant atoms (i.e. Ru or Sr separately). While in the case of adsorption mechanism, two different approaches were considered. Firstly, each dopant atom was adsorbed on the top layer of the surface and secondly, the depend atom was adsorbed inside the layer of surface. The grey spheres represent the titanium atoms, the red spheres represent the oxygen atoms, blue sphere represents Ru atom and green sphere represents Sr atom as shown in Figure 4.8 and 4.9.

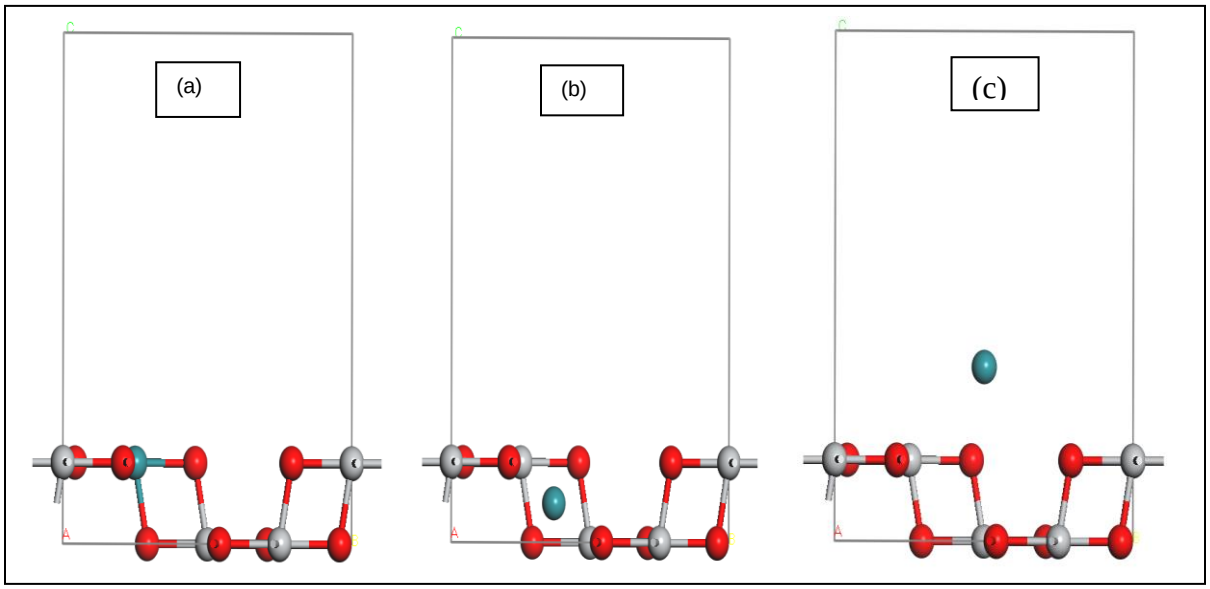

Figure 4.8 Structure of Ru-doped anatase TiO_2 (1 0 0) surface by replacing one Ti atom with Ru (a), adsorbing Ru atom (b) in side and (c) on top of the surface.

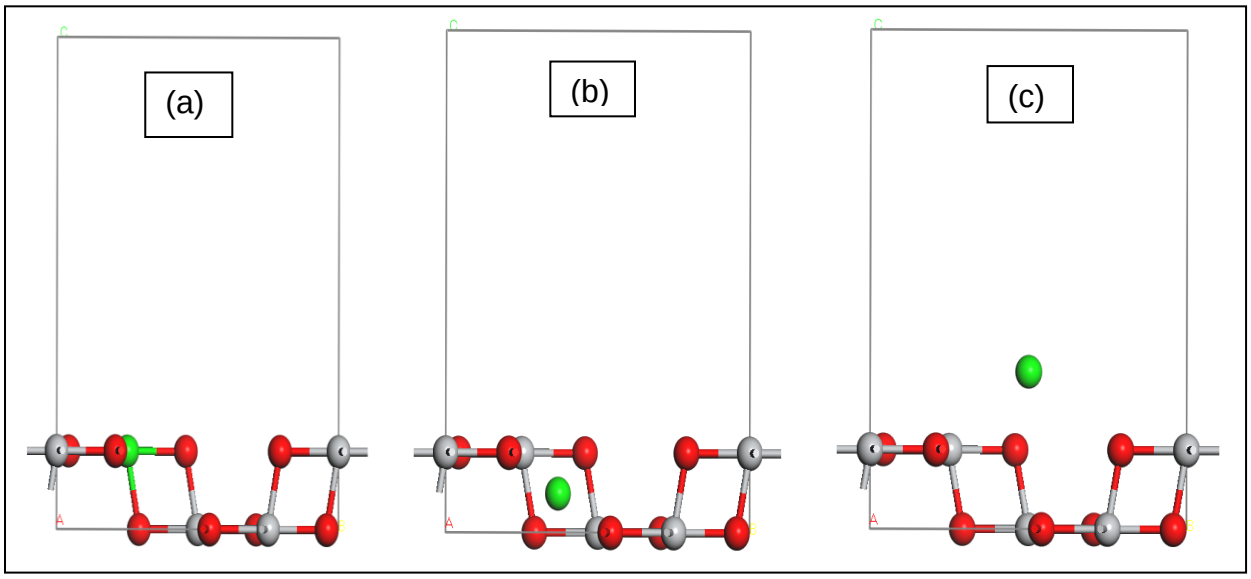

Figure 4.9 Structure of Sr-doped anatase TiO_2 (1 0 0) surface by replacing one Ti atom with Sr (a), adsorbing Sr atom (b) in side and (c) on top of the surface.

4.4 Electronic properties

4.4.1 Band structure and DOS of undoped anatase TiO_2 (1 0 0) surface

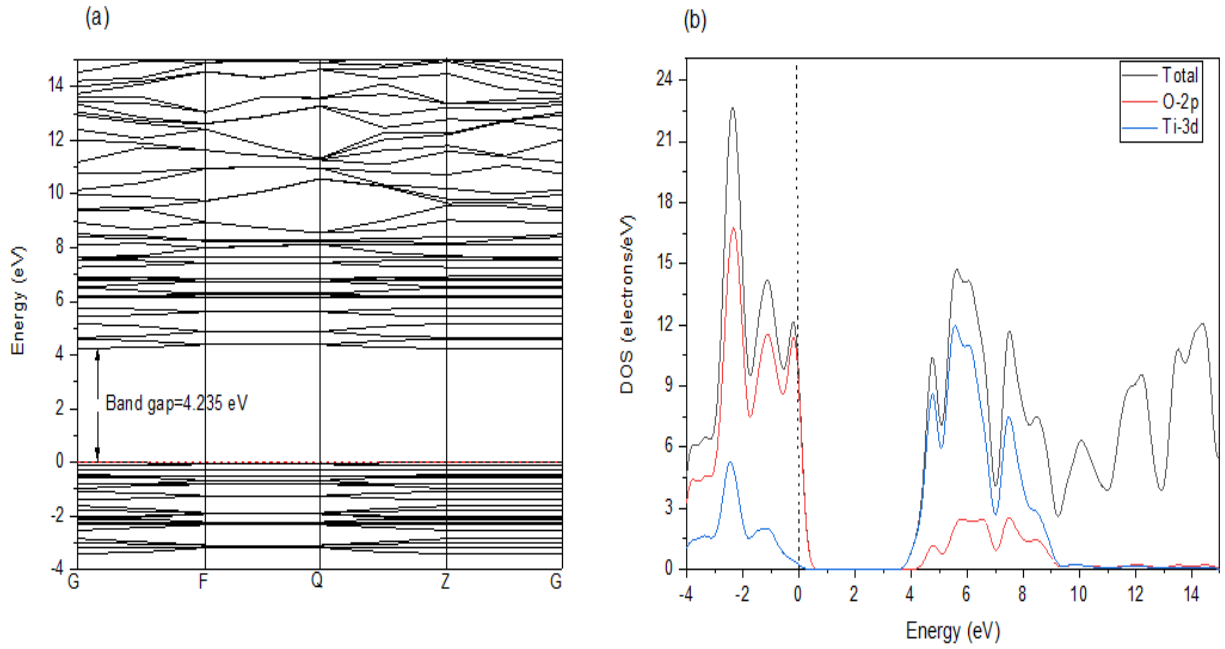

Figure 4.10 Band structure (a) and density of states (b) of undoped anatase TiO_2 (1 0 0) surface under the scissor operation.

The band gap values are determined by the energy range between VB and CB, and impurity states in the band gaps can reduce the electronic transition energy of a system. Figure 4.10 presents the band structure and DOS of undoped anatase TiO_2 (1 0 0) surface under the scissor operation. We set the same k-point mesh to sample the first Brillouin zone for the undoped, and Ru and Sr-doped anatase TiO_2 (1 0 0) surface models, which is to conveniently compare the doping effects of different doping elements and methods on the energy band structures of anatase TiO_2 (1 0 0) surface. The calculated energy band gap of undoped anatase (1 0 0) surface was found to be 3.128 eV, consistent with the experimental value of 3.230 eV. This difference of the calculated band gap from the experimental value can be attributed to the selection of exchange-correlation energy in DFT. Therefore, the scissor operation of 1.107 eV has been employed on all undoped, and Ru and Sr-doped anatase TiO_2 (1 0 0) surface to compensate for the underestimation of the energy band gap.

Figure 4.10 (a) shows that the band structure of undoped anatase TiO_2 (1 0 0) surface under the scissor operation displays a direct band gap about 4.230 eV. The dotted line is Fermi level. The top of the VB of undoped anatase TiO_2 (1 0 0) surface is near the Fermi level, which implies that undoped anatase TiO_2 (1 0 0) surface is p-type semiconductor. In Figure 4.10 (b) the VB is located between –4. 00 eV and the Fermi level was formed by the bonding states of the hybridized O-2p and Ti-3d states with a minor contribution from Ti-3p and Ti-4s states. The O-2p and Ti-3d states are major contribution for the VB. The CB located between 4.235 eV and 8.990 eV above the Fermi level was formed primarily by the Ti-3d states with a minor contribution from O-2p state. The CB also consists of O-2p and Ti-3d states.

4.4.2 Band structure of Ru and Sr-doped anatase TiO_2 (1 0 0) surface

Actually, there are many factors affecting the photocatalytic efficiency of TiO_2, in addition to external conditions (such as light source, time, temperature, and the pH value of reaction system), and also including intrinsic characteristics of TiO_2, especially specific surface area, impurity energy levels (IELs) bands and defects. In this study, mainly the effects of impurity bands are considered since the are important, especially those located between the Fermi level and the VB. Because this impurity band can act as a “step” to

reduce the electronic transition energy, it means that more electrons can be excited. More excited electrons mean greater probability that photo-excited electrons can migrate to the surface. Meanwhile, the IELs or band could also act as a separating center. The photo-excited electron-hole pair can separate rapidly and effectively, which will promote the carrier's diffusion and enhance the charge carrier lifetime. Therefore, the quantum transformation efficiency can be improved, which will lead to the enhancement of the photocatalytic efficiency of anatase TiO_2 (1 0 0) surface. To study the influence of doping on the electronic structures of anatase TiO_2 (1 0 0) surface, Ru and Sr-doped anatase TiO_2 (1 0 0) surface system were geometrically optimized until all the parameters were below the suitable tolerance criterion. The calculated energy band gap values for both Ru and Sr-doped anatase TiO_2 (1 0 0) surface systems are presented in Table 4.2 below.

Table 4.2 Comparison of the calculated energy band gaps (eV) and scissor operator (1.107 eV) of Ru- and Sr-doped anatase TiO_2 (1 0 0) surface structures modelled using two doping approaches.

Configuration	Band gap Ru-doped (eV)	Scissor operator (1.107 eV)	Band gap Sr-doped (eV)	Scissor operator (1.107 eV)
Ti Substitution	1.348	2.455	0.177	1.284
On-top adsorption	0.158	1.265	0.376	1.483
In-surface adsorption	1.194	2.301	0.501	1.608

Table 4.2 illustrates comparison of the calculated energy band gap and scissor operator (1.107 eV) of Ru- and Sr-doped anatase TiO_2 (1 0 0) surface. Ru-doped anatase TiO_2 (1 0 0) surface with both substitution and adsorption methods have the band gaps of 2.455 eV, 1.265 eV and 2.301 eV under scissor operator, while substitutional Ru-doped gave a larger energy band gap of 2.455 eV compared to adsorption method with the band gaps of 1.265 eV and 2.301 eV for on-top and in-surface adsorption respectively. On the other

hand, Sr-doped via both substitution and adsorption methods have the band gaps of 1.284 eV, 1.483 eV and 1.608 eV under the scissor operator, while substitutional Sr-doped gave a smaller energy band gap of 1.284 eV compared to adsorption approach with values of 1.483 eV for on-top and 1.608 eV for in-surface mechanism. It is noted that Ru and Sr-doped reduced the energy band gap as compared to undoped anatase TiO_2 (1 0 0) surface. The calculated band structures of Ru- and Sr-doped anatase TiO_2 (1 0 0) surface under the scissor operation are shown in from Figures 4.11 to 4.16.

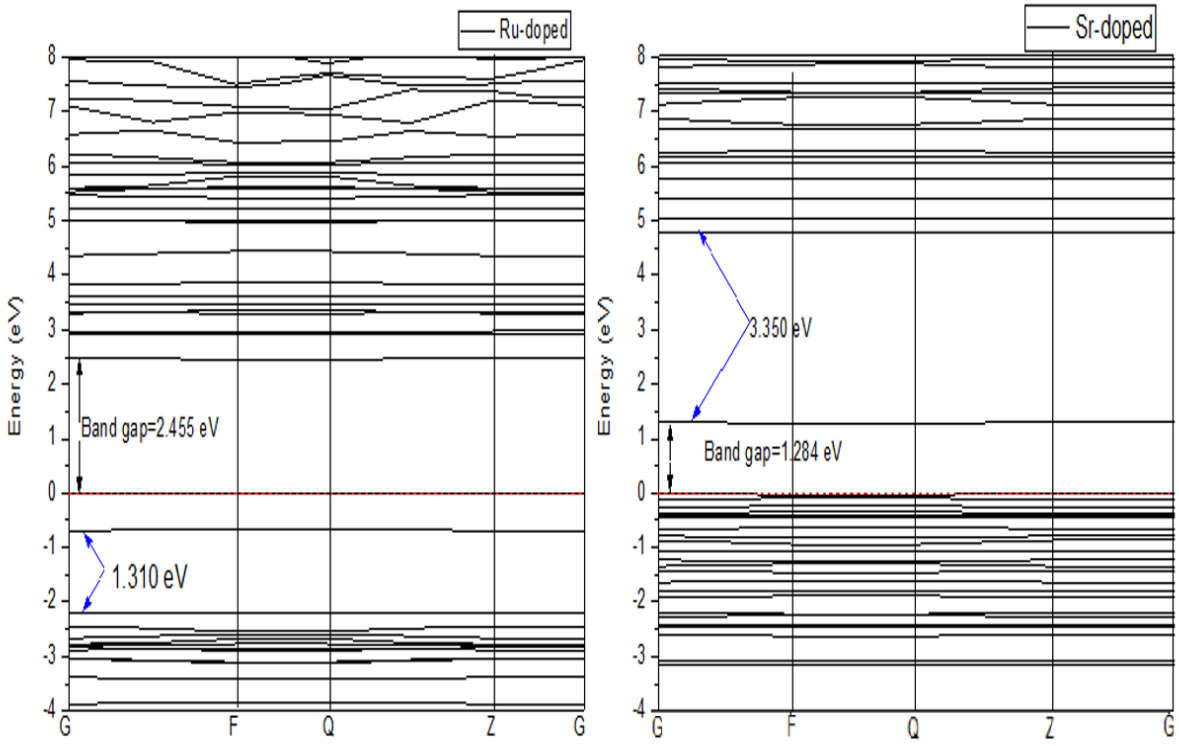

Figure 4.11 Band structure of Ru and Sr-doped anatase TiO_2 (1 0 0) surface by replacing one Ti atom with dopant atom under the scissor operation.

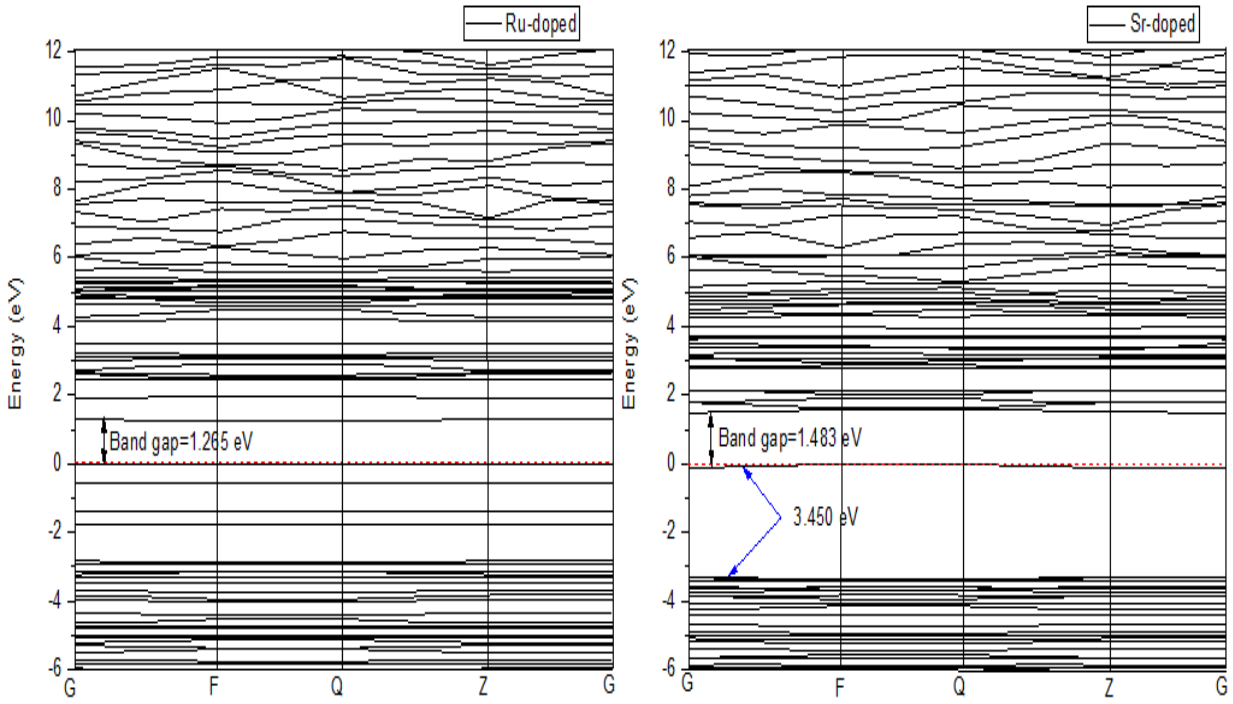

Figure 4.12 Band structure of Ru and Sr-doped anatase TiO_2 (1 0 0) surface by adsorbing dopant atom on top of the surface under the scissor operation.

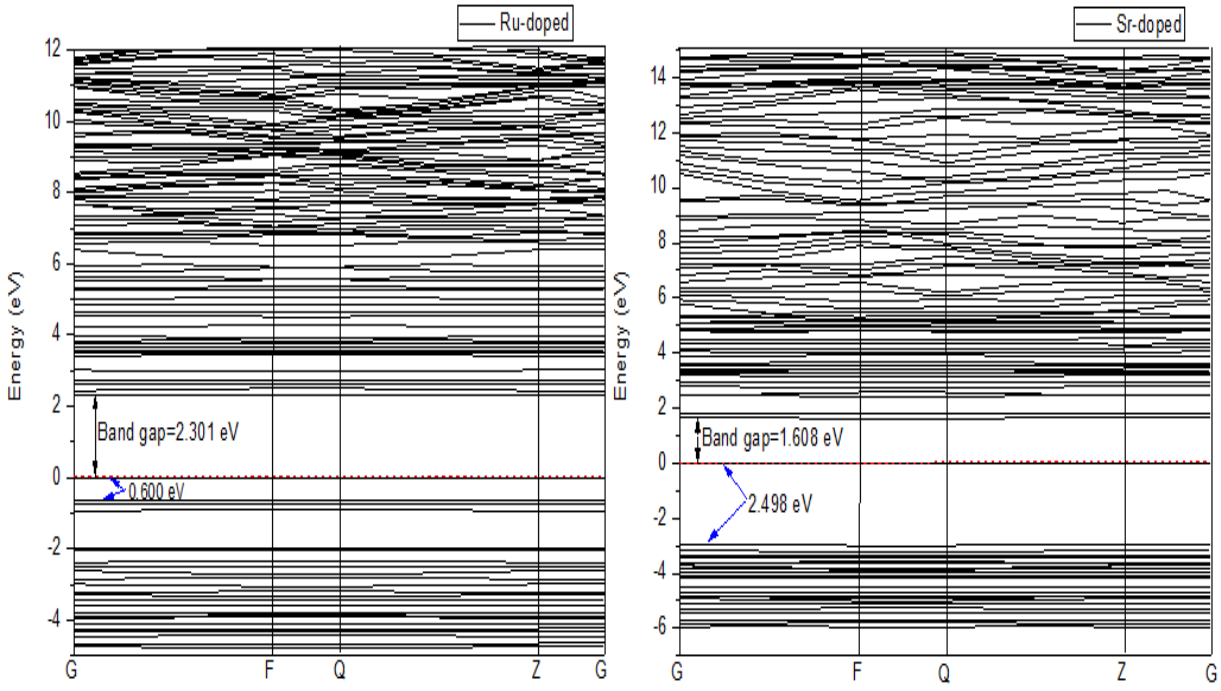

Figure 4.13 Band structure of Ru and Sr-doped anatase TiO_2 (1 0 0) surface by adsorbing dopant atom in surface under the scissor operation.

Figures 4.11 to 4.13 show that the VBs of Ru and Sr-doped shift toward the Fermi level, which implies that Ru- and Sr-doped anatase TiO_2 (1 0 0) surface is also a p-type semiconductor. This shifts the effective Fermi level to a point about halfway between the acceptor levels and the VB. Since the position of the Fermi level with respect to VB and CB depends on various parameters as the temperature, the effective masses of electrons and holes, and the number of free electrons and holes. Electrons can be elevated from the VB to the holes in the band gap with the energy provided by an applied voltage. Since electrons can be exchanged between the holes, the holes are said to be mobile. The holes are said to be the "majority carriers" for current flow in a p-type semiconductor.

Ru-doped anatase TiO_2 (1 0 0) surface by substitution has one IELs located in the VB, which is conducive to decreasing the energy band gap. The O-2p and Ru-4d states shift upward by a value of 1.310 eV as shown in Figure 4.11. On other hand, Ru-doped anatase TiO_2 (1 0 0) surface by adsorption on-top of the surfacehas no IELs in the forbidden band as shown in Figure 4.12, while Figure 4.13 shows that Ru-doped anatase TiO_2 (1 0 0) surface by in-surface adsorption has one small IELs located in VB near the Fermi level. The O-2p and Ru-4d states shift upward by a value 0.660 eV near the Fermi level. Therefore, two IELs are found, both lying under the Fermi level, but the one for value 0.660 eV is closer to the Fermi level.

Figure 4.11 shows that substitutionally Sr-doped anatase TiO_2 (1 0 0) surface has one IELs located in the CB, whereby Ti-3d and Sr-5s states shift downward by the value of 3.350 eV while Figure 4.12 shows that Sr-doped anatase TiO_2 (1 0 0) surface by on-top of the surface adsorption has IELs located in the VB. The O-2p states shift upward by a value of 3.450 eV. Figure 4.13 shows that Sr-doped anatase TiO_2 (1 0 0) surface by in-surface adsorption has one IELs located in VB and O-2p states shift upward by a value 2.498 eV. Three IELs are found, one lies on the top of the Fermi level and the other two lie under the Fermi level, which are helpful for decreasing the band gap.

Essentially, several IELs appear between the VB and CB of all the doped systems, which not only reduce the electronic transition energies but also affect the recombination rate of electron–hole pairs, which influence the visible-light absorption and photocatalytic activity of materials under visible-light. Moreover, Ru- and Sr-doped systems show a pronounced

narrowing of band gap with the average of 2.008 eV and 1.450 eV respectively as compared to band gap 4.235 eV of undoped (1 0 0) surface of anatase TiO_2 under the scissor operation. Furthermore, the study suggests that the rate of the electron transfer from the VB to the CB is enhanced, due to the reduction in energy band gap of doped systems as compared to undoped system. DFT is still a widely accepted method to depict the defects states in the electronic structure calculations, and this gives reasonable explanation for the experimental results because only the relative position of the occupies states and empty states need considering.

4.4.3 DOS of Ru- and Sr-doped anatase TiO_2 (1 0 0) surface

In order to further analyze the composition of VB and CB, and better understand the changes of electronic structure, the total density of states and partial density of states of Ru and Sr- doped anatase TiO_2 (1 0 0) surface were calculated using GGA. The Fermi level was set as the highest filled level of the electrons. The corresponding TDOS and PDOS of Ru and Sr-doped anatase TiO_2 (1 0 0) surface under the scissor operation are shown in Figures 4.14 to 4.16.

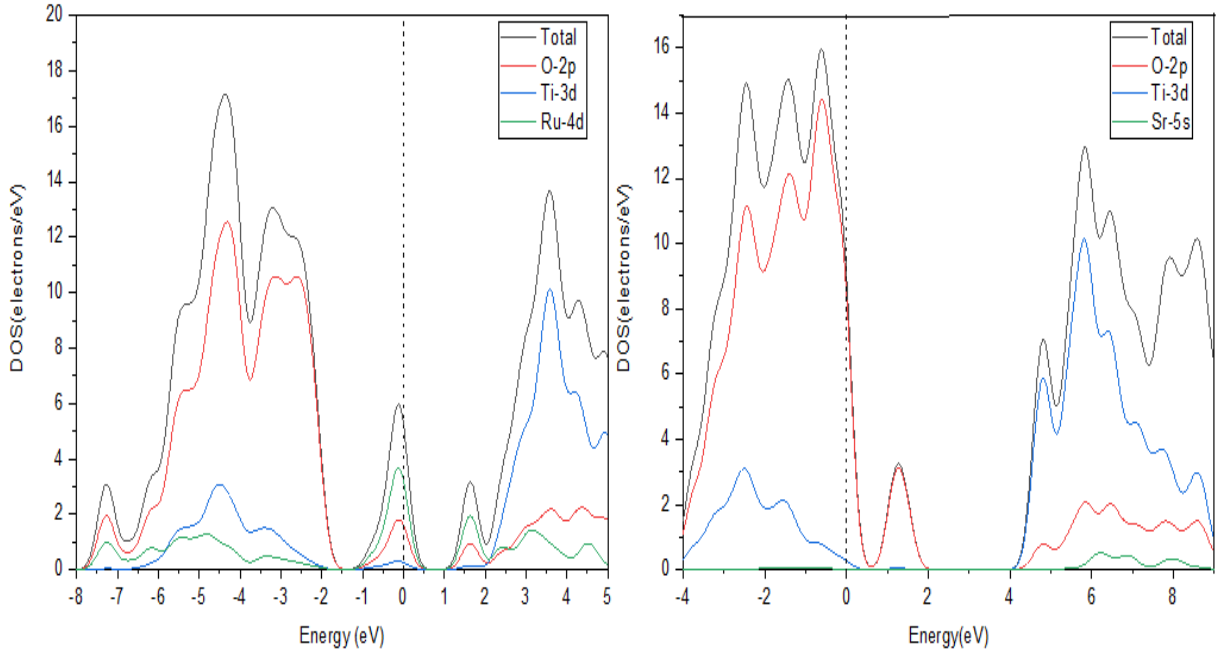

Figure 4.14 DOS of Ru and Sr-doped anatase TiO_2 (1 0 0) surface by replacing one Ti atom with dopant atoms under the scissor operation.

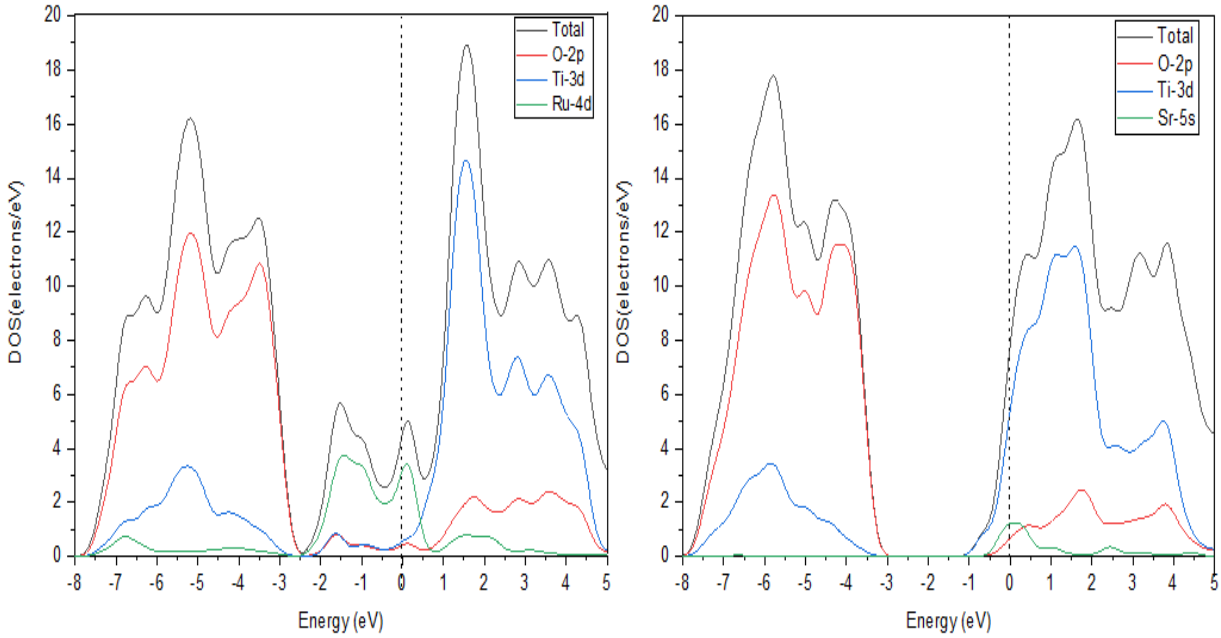

Figure 4.15 DOS of Ru and Sr-doped anatase TiO_2 (1 0 0) surface by adsorbing dopant atom on top of the surface under the scissor operation.

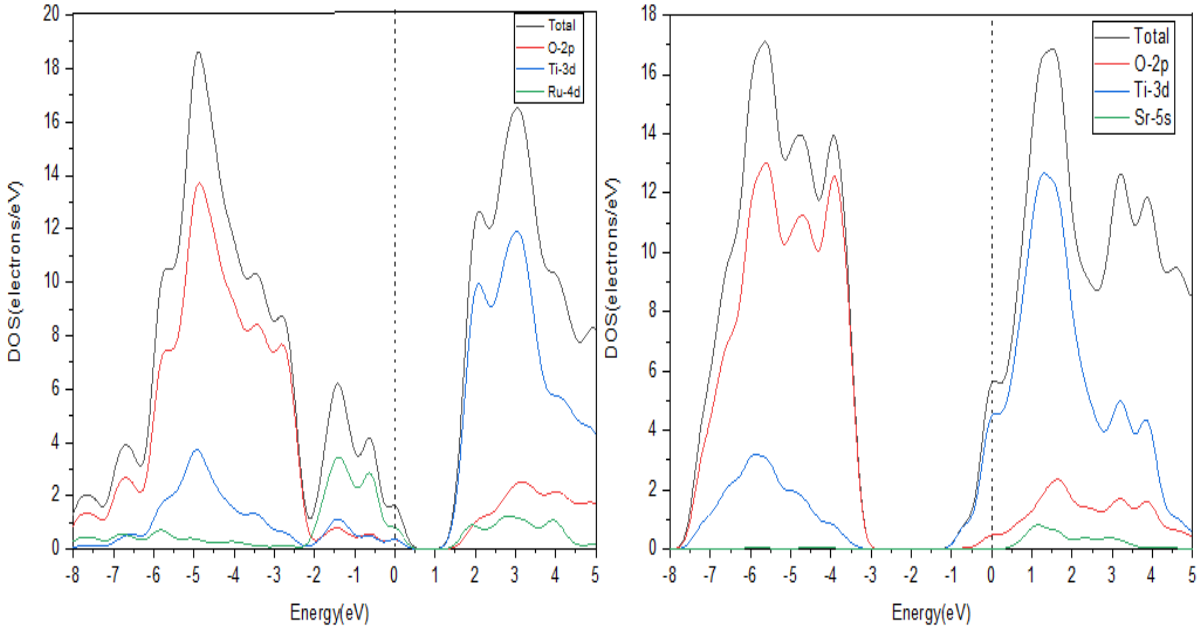

Figure 4.16 DOS of Ru- and Sr-doped anatase TiO_2 (1 0 0) surface by adsorbing dopant atom in the surface under the scissor operation.

Various doping mechanisms shown in Figures 4.14 to 4.16 revealed that the VB of Ru-doped anatase TiO_2 (1 0 0) surface has been formed by the bonding states of the hybridized O-2p, Ti-3d and Ru-4d states with minor contributions from Ru-4d, Ti-3p and Ti-4s states. The CB of Ru-doped anatase TiO_2 (1 0 0) surface above the Fermi level is formed primarily by the Ti-3d states with minor contributions from O-2p and Ru-4d states. On the other hand, the VB of Sr-doped anatase TiO_2 (1 0 0) surface has been formed by the bonding states of the hybridized O-2p and Ti-3d states with minor contributions from Ti-3p and Ti-4s states. There are no peaks for Sr-5s states in VB region. The CB of Sr-doped anatase TiO_2 (1 0 0) surface above the Fermi level is formed primarily by the Ti-3d orbitals with minor contributions from O-2p and Sr-5s states. This indicates that the electrons and holes can be separated effectively and then improve the photocatalytic efficiency of anatase TiO_2 due to the energy levels crossed with each other at the bottom of the CB.

For Ru- and Sr-doped anatase (1 0 0) surface, a series of IELs (Ru-4d and Sr-5s) appear in the forbidden gap and all of IELs are located above the valence band maximum (VBM) and below the conduction band minimum (CBM) as shown from Figures 4.14 to 4.16. However, the excitation energy from the occupied states above the VBM to CBM should be much smaller than optical absorption energy of undoped anatase TiO_2, which can explain why Ru- and Sr-doped anatase TiO_2 (1 0 0) surface has better visible-light photocatalytic activity and a red-shift of optical absorption compared to undoped anatase TiO_2 (1 0 0) surface. Since Ru- and Sr-doped anatase TiO_2 reduced the energy band gap, as a consequence, the electrons transition from isolated state to the CB would lead to an obvious reduction of absorption energy, which also gives a good explanation for experimentally observed red-shift of the absorption edge. Hence, the shift of the optical absorption edge corresponds to a decrease of absorption energy.

4.5 Optical properties of Ru and Sr-doped anatase TiO_2 (1 0 0) surface

The optical properties for a given system are commonly defined by its band gap, which is the energy difference between the highest occupied (or VBM) and lowest unoccupied (or CBM) densities of states for the same, and this energy separation between the two states defines its sensitivity/responsivity to the solar spectrum.

4.5.1 Optical absorption

The absorption coefficient determines how far light of a particular wavelength can penetrate into a material before it is absorbed. The energy and wavelength of absorption can be defined by difference between energy levels of an electronic transition. In order to explore the absorption properties, the optical absorption spectra of undoped and Ru- and Sr-doped anatase TiO_2 (1 0 0) surface were calculated on the basis of the detailed electronic band structure as shown in Figures 4.17 to 4.19.

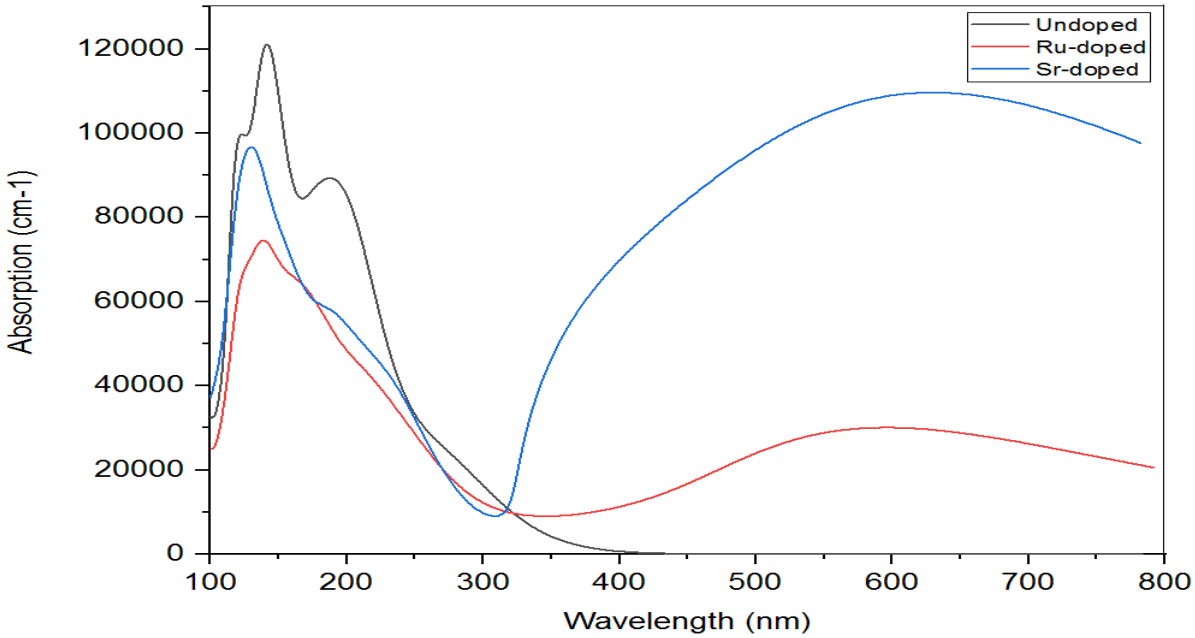

Figure 4.17 The absorption coefficient of undoped and substitutional Ru- and Sr-doped anatase TiO_2 (1 0 0) surface

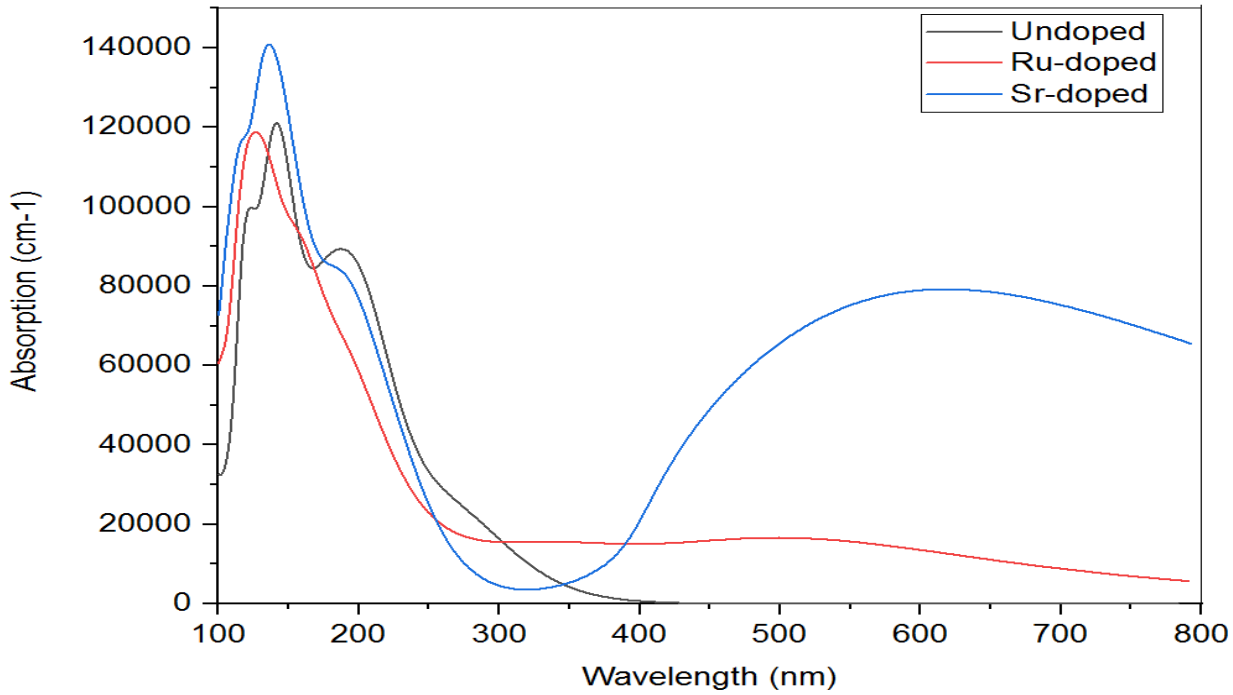

Figure 4.18. The absorption coefficient of undoped and Ru and Sr-doped anatase TiO_2 (1 0 0) surface by dopant atom on top of the surface.

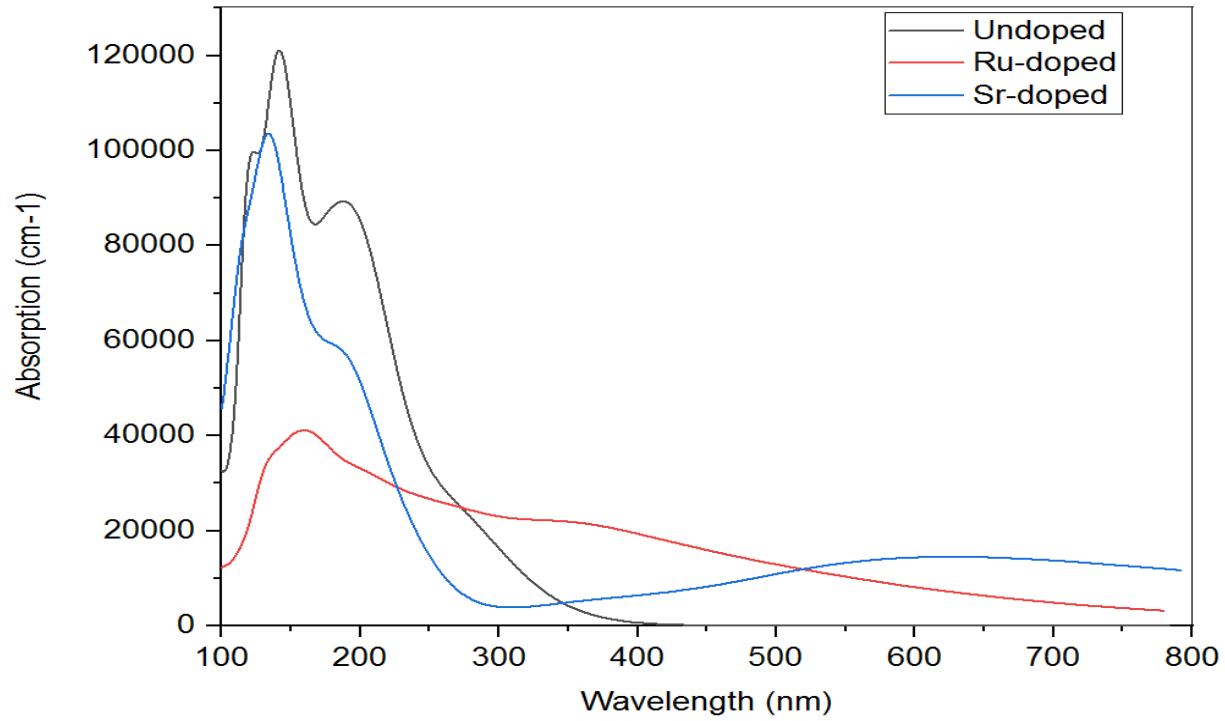

Figure 4.19 The absorption coefficient of undoped and Ru and Sr-doped anatase TiO_2 (1 0 0) surface by dopant atom in the surface.

The optical absorption of undoped, Ru- and Sr-doped anatase TiO_2 (1 0 0) surface under the scissor operation are shown in Figures 4.17 to 4.19. Due to the underestimation of the band gap, it is difficult to obtain the exact optical band gap. This scissor operator can effectively describe the difference between the theoretical and experimental band gap values. When the experimental value is known, we can perform a band structure calculation to find the theoretical band gap. The relative position of the conduction to valence band is erroneous when the Kohn-Sham eigenvalues are used. In an attempt to fix this problem, inherent in DFT, we allow a rigid shift of the conduction levels to be consistent with the measured value of the band gap. In our calculation, the band gap of bulk anatase TiO_2 is 2.123 eV, which is underestimated by 1.107 eV compared with experimental data. Therefore, the 1.107 eV scissors operator has been used to evaluate the optical absorption. Compared with the undoped anatase TiO_2 (1 0 0) surface, it is obvious that the sparsely doped Ru and Sr atoms contribute to the in-gap impurity bands, while having few effects on the host's DOS. Therefore, the same scissor operator is applied to the doped anatase TiO_2 (1 0 0) surface systems. This method is effective for a variety of systems [37-40]. It can be observed from Figures 4.17 to 4.19 that the Ru and Sr-doped anatase TiO_2 (1 0 0) surface by substitution and adsorption mechanisms show the enhancement of visible light absorption.

Substitutional doping revealed that Sr-doped anatase TiO_2 (1 0 0) surface presents the overall optical absorption in the range of 330-800 nm, and the absorption center of Sr-doped anatase TiO_2 (1 0 0) surface is located at 645 nm. The results show that the Sr doping can promote the visible optical absorption of anatase TiO_2. Thus, if the preparation methods can be controlled appropriately, the Sr-doped anatse TiO_2 (1 0 0) surface can enhance the visible light response and the absorption band edge shifts to the long wavelength region. Similarly, the substitutional Ru-doped anatase TiO_2 (1 0 0) surface also shows evident visible absorption. The absorption center of Ru-doped anatase TiO_2 (1 0 0) surface is located at around 600 nm. Therefore, Ru and Sr-doped anatase TiO_2 (1 0 0) surface presents the slight enhancement in the visible region compared with the undoped anatase TiO_2 (1 0 0) surface. But Sr-doped has higher absorption on visible spectrum compared with Ru-doped as shown in Figure 4.17. This implies that the Sr-

doped anatase TiO_2 (1 0 0) surface probably has a higher photocatalytic activity by substitution method, because of the larger value of IELs.

Doping by adsorption method shown in Figure 4.18 shows that Sr-doped anatase TiO_2 (1 0 0) surface has stronger light absorption in the range of 390-800 nm compared with Ru-doped anatase TiO_2 (1 0 0) surface and the absorption center of Sr-doped is located at 640 nm. Ru-doped shows a small light absorption which is decreasing toward visible light. Figure 4.19 shows that Ru-doped anatase TiO_2 (1 0 0) surface has optical absorption in the range of 300-800 nm, which is decreasing toward the visible light. Similarly, Sr-doped anatase TiO_2 (1 0 0) surface presents optical absorption in the range of 300-800 nm, which is increasing toward the visible light. It was found that the optical absorption curves of Ru and Sr-doped anatase TiO_2 (1 0 0) surface, show red shifts toward the visible light region. Therefore, Ru- and Sr-doped shows the highest visible light absorption compared to undoped anatase TiO_2 (1 0 0) results from the dopant states in gap. Through comparison and analysis, it is concluded that the synergistic effects of Ru and Sr dopant atoms are the main reasons that cause the anatase TiO_2 (1 0 0) surface energy band gap narrowing and improving the visible light photocatalytic.

4.5.2 Reflection and energy loss function

The loss function and reflectivity of undoped, Ru and Sr-doped anatase TiO_2 (1 0 0) surface by substitution, on-top and in-surface doping are presented in Figures 4.20 to 4.22. The loss function is energy loss of electrons when passing through uniform dielectric material. The major peak of energy loss function for undoped anatase TiO_2 (1 0 0) surface is positioned at 11.00 eV. This major peak is higher than those of Ru and Sr-doped anatase TiO_2 (1 0 0) surface for both methods. For substitutional doping the major peak is located at 11.00 eV and 10.50 eV for Ru and Sr-doped respectively. Then for in surface adsorption, the major peak is positioned at 7.75 eV and 11. 25 eV for Ru and Sr-doped respectively. Lastly, for the on-top adsorption the major peak is located at 12.00 eV and 11.20 eV for Ru and Sr-doped respectively as shown in Figure 4.22. Therefore, the study suggests that Ru and Sr-doped anatase TiO_2 (1 0 0) surface has less energy loss of electrons, because of shorter major peaks compared to undoped anatase TiO_2 (1 0 0) surface.

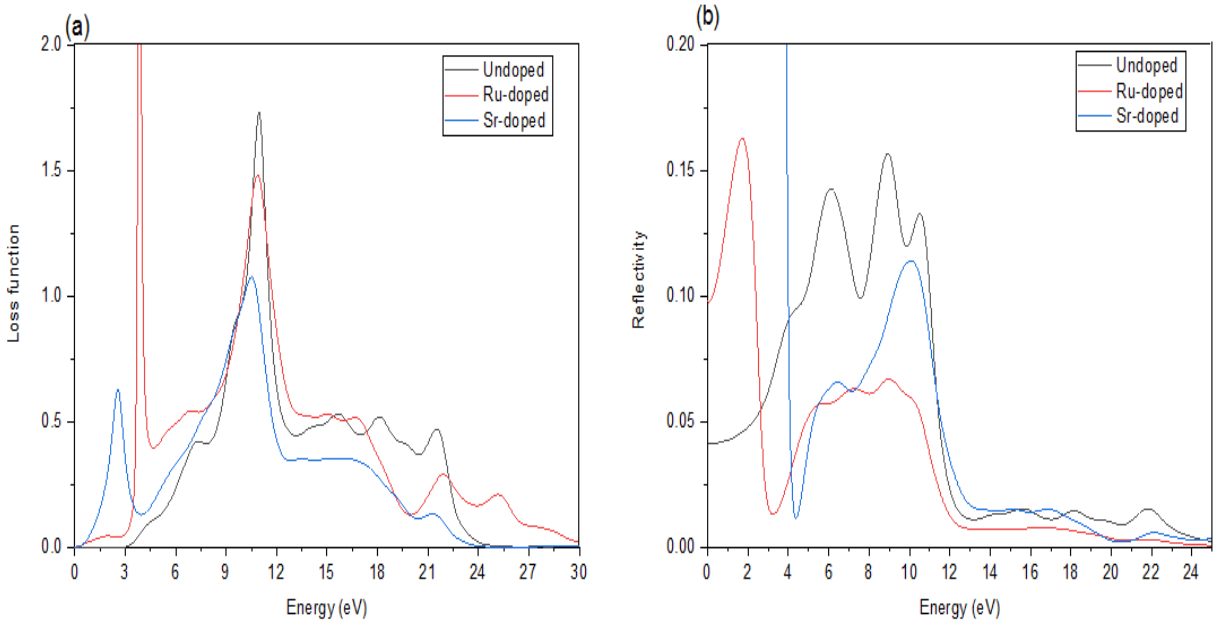

Figure 4.20 (a) Loss function and (b) reflectivity of undoped, Ru and Sr-doped anatase TiO_2 (1 0 0) surface by substitution.

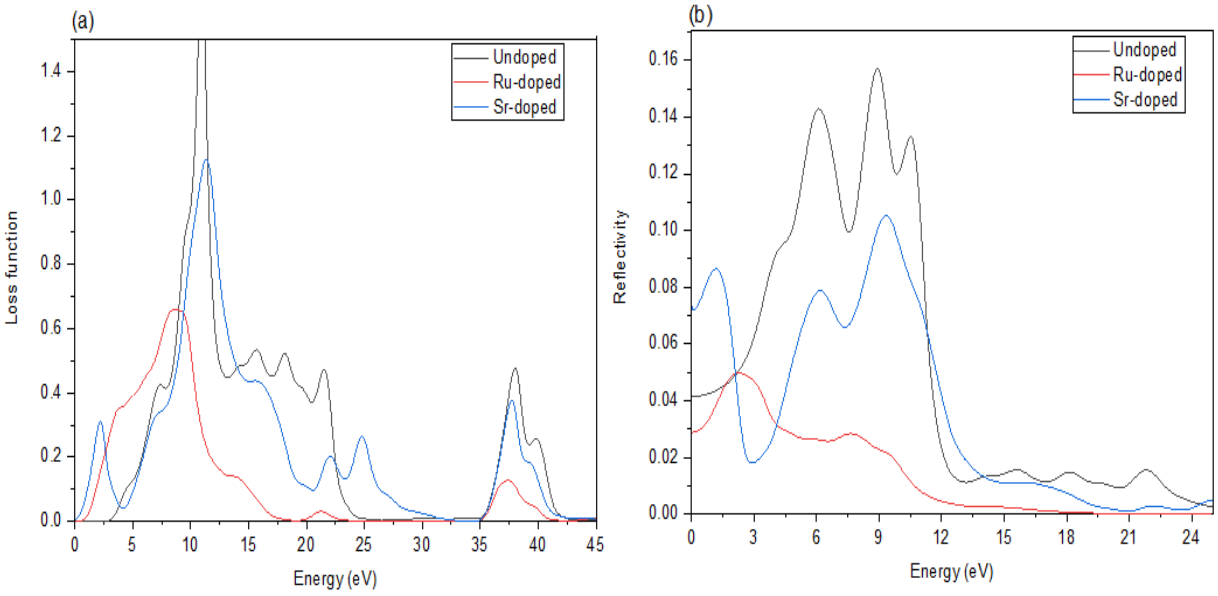

Figure 4.21 (a) Loss function and (b) reflectivity of undoped, Ru and Sr-doped anatase TiO_2 (1 0 0) surface by dopant atom in the surface.

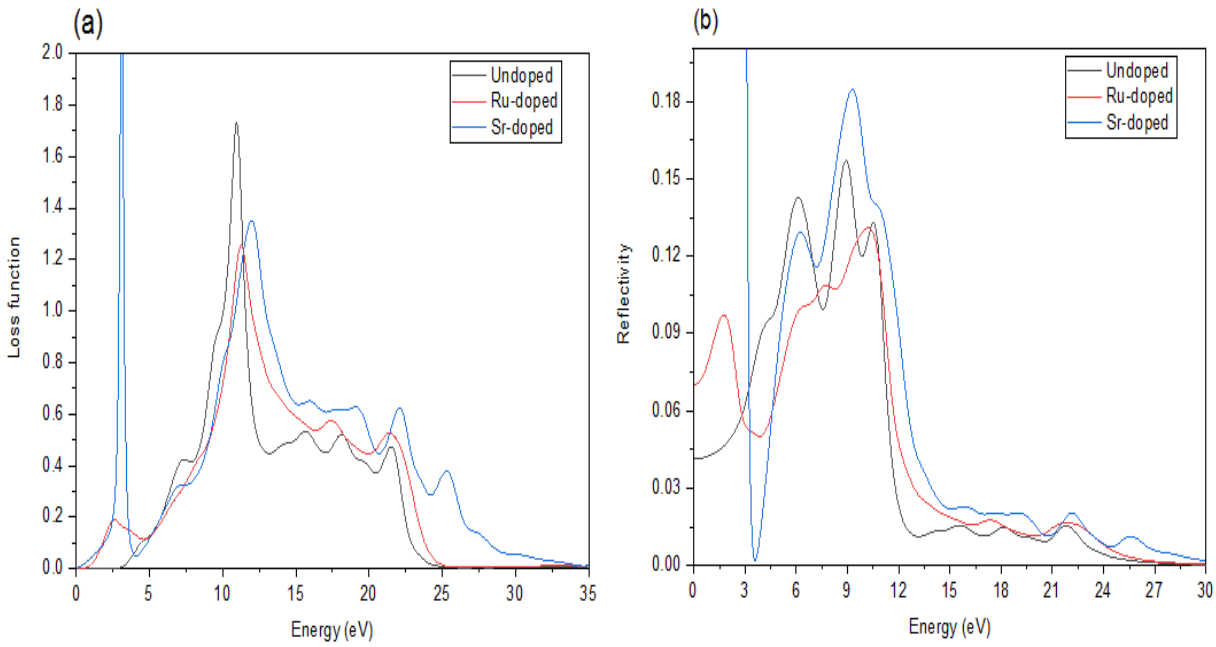

Figure 4.22 (a) Loss function and (b) reflectivity of undoped, Ru and Sr-doped anatase TiO_2 (1 0 0) surface by dopant atom on top of the surface.

Reflectivity is an optical property of material, which describes how much light is reflected from the material in relation to an amount of light incident on the material [87]. The reflection occurs always on the surface of the material, for the light-diffusing (translucent) materials also in the volume of the material. Reflectivity depends on the wavelength of light, direction of the incident and reflected light, polarization of light, type of the material (metal, plastic, etc.), chemical composition and structure of the material, and state of the material and its surface (temperature, surface roughness, degree of oxidation and contamination). Figures 4.20 (b) to 4.22 (b) show that the undoped, Ru and Sr-doped anatase TiO_2 (1 0 0) surface systems in the energy ranges of ~0–13.50 eV have strong light reflected and it is also noted that between energy ranges of ~13.50–24.00 eV small amount of light is reflected. This may be due to the Ru and Sr impurities added onto the surface.

4.5.3 Dielectric function and refractive index

To investigate the optical band gap and optical transition of undoped Ru- and Sr-doped TiO_2 (1 0 0) surface, it is necessary to elucidate the imaginary part of the dielectric function

$\varepsilon_2(\omega)$, because $\varepsilon_2(\omega)$ is important for describing the optical properties of any material. It is well known that the interaction of a photon with electrons in a material can be described in terms of time-dependent perturbations of the ground-state electronic states. The spectra from the excited states can be described as a joint density of states between the VB and CB. The momentum matrix elements, which are used to calculate $\varepsilon_2(\omega)$, are calculated between occupied and unoccupied states, which are given by the eigenvectors obtained as solution of the corresponding Schrödinger equation.

To evaluate these matrix elements, one uses the corresponding eigenfunctions of each of the occupied and unoccupied states. The dielectric function spectrum is an important indicator for any material to describe the optical response. Optical transitions between occupied and unoccupied states are caused by the electric field of the photon. The spectra from the excited states can be described as a joint DOS between the VB and CB. Optical transition peaks correspond to optical transitions between two states, and intensity of peaks is proportional to density of states. The transition in photosensitivity of the anatase TiO_2 (1 0 0) surface from the UV to the visible wavelength range upon Ru- and Sr-doping is attributed to electronic transitions between the VB and dopant-induced impurity state or between the impurity state and the CB. The calculated imaginary parts of dielectric function and real parts of refractive index of undoped and Ru- and Sr-doped anatase TiO_2 (1 0 0) surface are shown in Figures 4.23 to 4.25.

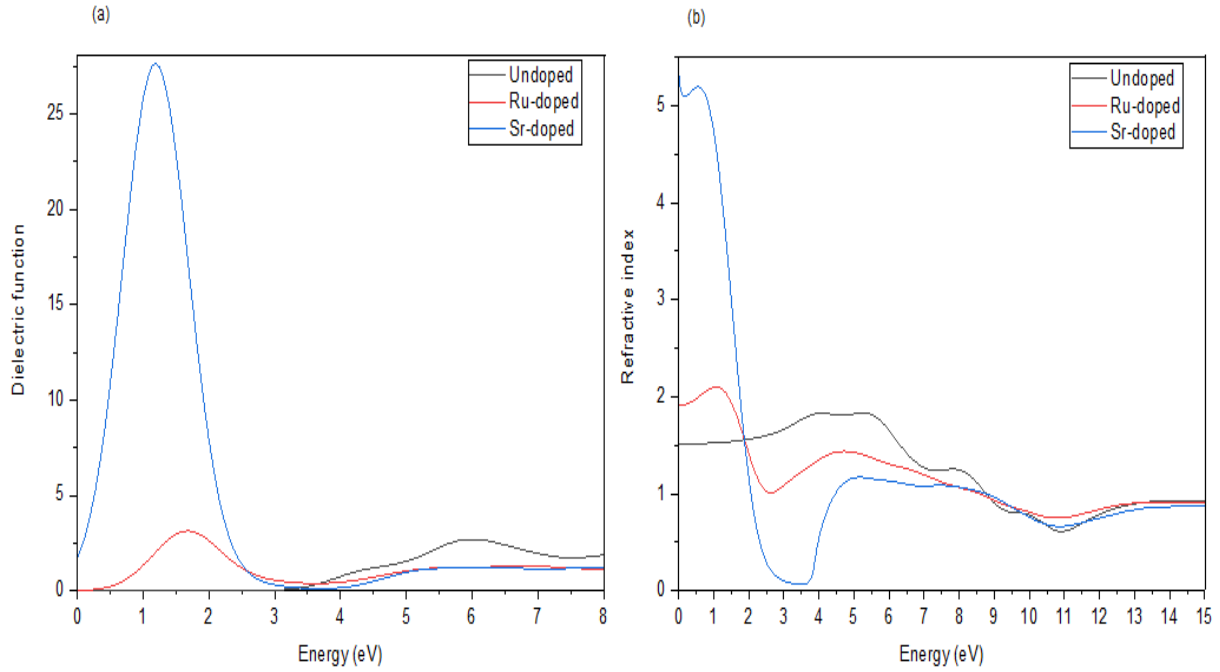

Figure 4.23 (a) Imaginary part of dielectric function and (b) real part of refractive index of undoped and Ru- and Sr-doped anatase TiO_2 (1 0 0) surface by substitution.

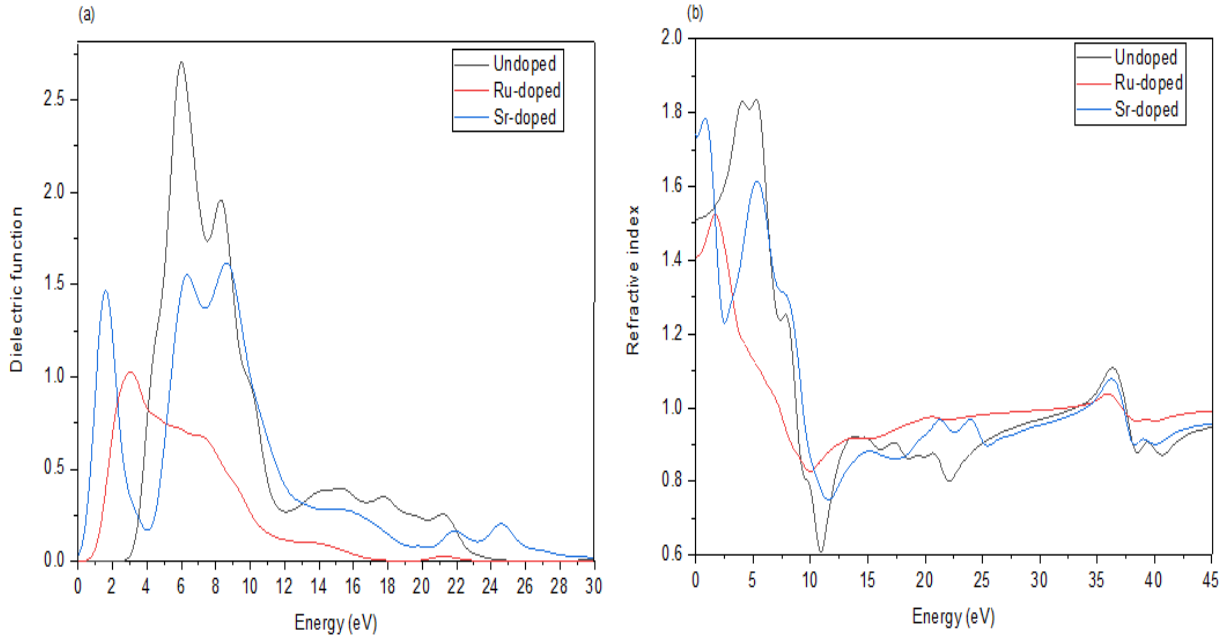

Figure 4.24 (a) Imaginary part of dielectric function and (b) real part of undoped and Ru- and Sr-doped anatase TiO_2 (1 0 0) surface by on-top adsorption.

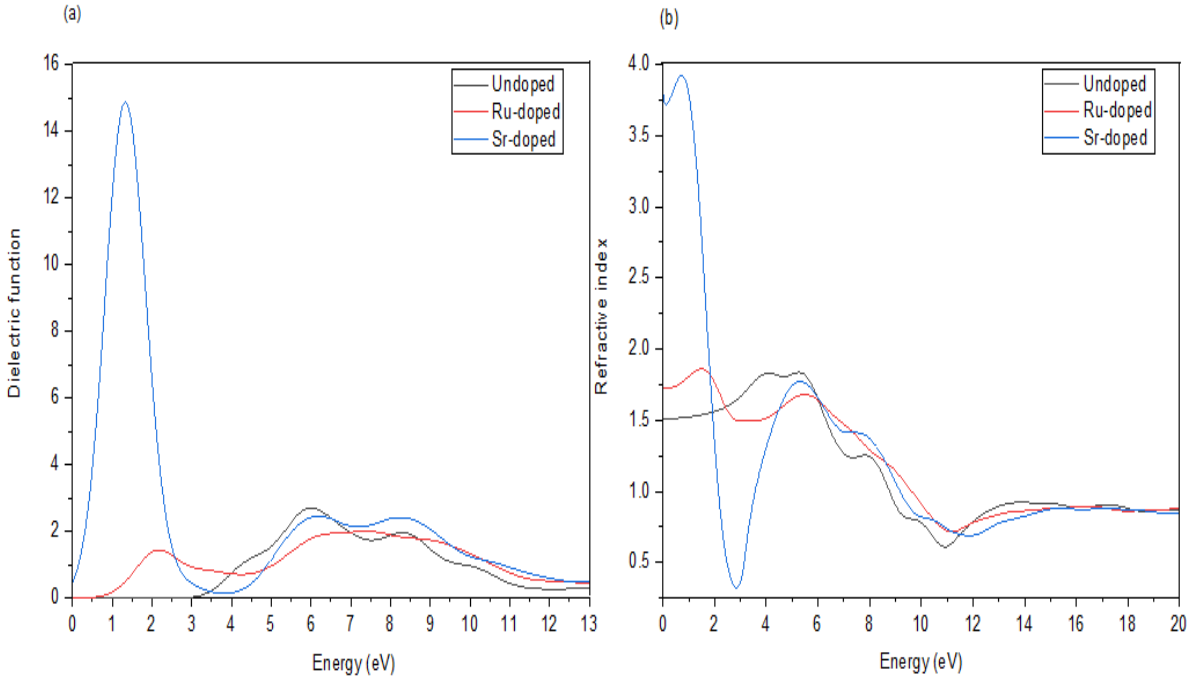

Figure 4. 25 (a) Imaginary part of dielectric function and (b) real part of refractive index of undoped and Ru and Sr-doped anatase TiO_2 (1 0 0) surface by in-surface adsorption.

To illustrate the optical transition mechanism in detail, the imaginary part of dielectric function and real part of refractive index of undoped, Ru- and Sr-doped anatase TiO_2 (1 0 0) surface are presented in Figures 4.23 to 4.25. It is well-known that the imaginary part of dielectric function can describe the optical transition well. The real part of the refractive index is calculated in the polarization direction. It was found that the undoped anatase TiO_2 (1 0 0) surface shows the optical transition of 6.00 eV, which is related to the intrinsic transition between O-2p states at the VB and Ti-3d states at the CB as shown in Figures 4.23 (a) to 4.25 (a) for various mechanisms. The computed highest peak of real part refractive index is 5.90 eV and is shown in Figures 4.23 (b) to 4.25 (b).

After doping, the intrinsic optical transition shows that there is a shift to the low energy range, implying that the band gaps are narrowed by doping with both Ru and Sr separately. The detailed optical transitions of Ru- and Sr-doped anatase TiO_2 (1 0 0) surface by substitution are found to be 1.55 eV and 1.25 eV respectively. It is worth noting that these imaginary peaks for Ru- and Sr-doped anatase TiO_2 (1 0 0) surface are attributed to the electronic transition from O-2p and Ru-4d states of the VB into the Ti-3d

and Ru-4d of the CB and attributed to the electronic transition from O-2p of the VB into the Ti-3d and Sr-5s of the CB respectively. Their computed highest peaks of real part refractive index are 1.18 eV and 1.00 eV as shown in Figure 4.23 (a) and (b) respectively. Ru- and Sr-doped anatase TiO_2 (1 0 0) surface by on-top adsorption shows the optical transitions of 3.10 eV and 9.50 eV, with highest peaks of real part refractive index of 1.70 eV and 1.55 eV as shown in Figure 4.24 (a) and (b) respectively. Combining with the previous electronic states and absorption results it can be concluded that the 3.10 eV and 9.50 eV peaks originate from the transition between the Ru-4d and Sr-5s states in the band gap and CB of Ru and Sr-doped anatase TiO_2 (1 0 0) surface. As for Ru and Sr-doped anatase TiO_2 (1 0 0) surface by in-surface, the visible optical transitions of 7.50 eV and 1.50 eV are revealed, which are attributed to the transition from the VB to the midgap states of Ru-4d and Sr-5s states as shown in Figure 4.25 (a) and (b) respectively. The real part of the refractive index are 1. 50 eV for Ru-doped and 0.75 eV for Sr-doped as shown in Figure 4.25 (b).

Furthermore, the position of imaginary peaks and real peaks of both Ru- and Sr-doped anatase TiO_2 (1 0 0) surface indicate strong interactions between electrons and photons, which would lead to more absorption. The Ru- and Sr-doped impurity increases the electrons transport as it reduces the energy band gap. Thus, the added impurity band reduces the electronic transition energy, which implies that more electrons can be excited. More electrons excitation increases the probability of more photo excited electron to be injected on the anatase TiO_2 semiconductor. This will promote more electrons to reach the photo electrode and an increase in the efficiency of DSSCs.

Chapter 5

5. Conclusion

The calculated lattice parameters of bulk anatase TiO_2 correlate very well with the reported theoretical and experimental results from the literature, with a deviation of 0.02% along a=b-axis and 0.22% along the c-axis and 0.02% along a=b-axis and 0.23% along the c-axis respectively. The calculated electronic band gap of bulk anatase TiO_2 is 2.123 eV. The optical properties of bulk anatase TiO_2 calculated within DFT are in good agreement with previous theoretically results. The optical absorption of bulk anatase TiO_2 occur in the UV light region at an absorption edge from 100 to 400 nm, with a small absorption decreasing toward visible light. This can contribute to the ability of TiO_2 to absorb light in weak or diffuse condition. This light can be shifted to a longer wavelength range by various methods such as doping TiO_2 surfaces. In this study anatase TiO_2 low index (1 0 0) surface doped with Ru and Sr was successfully investigated in order to understand how the light shift to a longer wavelength range. All the undoped, Ru- and Sr-doped anatase TiO_2 (1 0 0) low index surface calculations and results were discussed in detailed.

The energy plane-wave pseudopotential method implemented in DFT has been employed successfully to investigate the electronic properties and optical properties of undoped, and Ru- and Sr-doped anatase TiO_2 (1 0 0) surface. It was found that the Ru- and Sr-doped anatase TiO_2 (1 0 0) surface has higher photocatalytic ability than undoped anatase TiO_2 (1 0 0) surface. The results of doped systems showed that the energy band gaps and the carrier mobility in the VB, CB and IELs have a synergetic influence on the visible-light absorption and photocatalytic activity of the Ru- and Sr-doped anatase TiO_2 (1 0 0) surface. The impurity states between the VB and CB enhance the visible light absorption of Ru- and Sr-doped systems. The number and the carrier mobility of impurity level jointly influence the photocatalytic activity of catalyst under visible-light. Thus, the Sr-doping system shows higher photocatalytic activity than the Ru-doping system, because large amount of IELs are formed by the hybridization between Sr-5s states and Ti 3d and O 2p states, which is advantageous to extend the visible light absorption range in Sr-doped anatase TiO_2 (1 0 0) surface system. This doping mechanism opens a new

way of improving the optical absorption coefficient under visible light and provide insightful information for the design of visible photocatalytic materials.

References

[1] P. C. Choubey, A. Oudhia, R. Dewangan, and V. Y. T. P. G. Autonomous, Solar cell current scenario and future trends," *Recent Res. Sci. Technol.* , vol. 4, no. 8, pp. 99–101, 2012.

[2] M. T. Kibria, A. Ahammed, S. M. Sony, and F. Hossain, "A Review : Comparative studies on different generation solar cells technology," *Int. Conf. Environ. Asp. Bangladesh*, pp. 51–53, 2014.

[3] S. Sharma, K.K. Jain and A. Sharma, A. Solar Cells: In research and applications, A Review. Materials Sciences and Applications, *Scientific Research*. 6, 1145-115, 2015.

[4] S. Philipps, F. Ise, and W. Warmuth, "Fraunhofer ISE: Photovoltaics Report," July, 2017.

[5] IRENA, "Renewable Power Generation Costs in 2014 : An Overview," *Irena*, January, p. 92, 2015.

[6] Y. Jiao, F. Zhang, and S. Meng, "Dye sensitized solar sells principle and new design," *Int. J. Mol. Sci.*, vol. 11, no. 3, pp. 5–37, 1991.

[7] Y. Yang, Y. H. Qiang, J. Song, Z. Xing, and C. B. Song, "Enhanced charge-transfer performance of photoelectrode based on interface modification in dye-sensitized solar cells," *Int. J. Electrochem. Sci.*, vol. 10, no. 7, pp. 5479–5487, 2015.

[8] M. O'regan dan Grätzel, "A low cost, high efficiency solar cell based on dye-sensitized colloidal TiO_2 films," *Nature*, vol. 353, no. 6346, pp. 737–740, 1991.

[9] S. T. Kochuveedu, "Photocatalytic and photoelectrochemical water splitting on TiO_2 via photosensitization," *J. Nanomater.*, vol. 2016, 2016.

[10] B. E. Hardin, H. J. Snaith, and M. D. McGehee, "The renaissance of dye-sensitized solar cells," *Nat. Photonics*, vol. 6, no. 3, pp. 162–169, 2012.

[11] C.-K. Cheng, J.-Y. Lin, K.-C. Huang, T.-K. Yeh, and C.-K. Hsieh, "Enhanced efficiency of dye-sensitized solar counter electrodes consisting of two-dimensional nanostructural molybdenum disulfide nanosheets supported Pt nanoparticles," *Coatings*, vol. 7, no. 10, p. 167, 2017.

[12] E. Stathatos, "Dye sensitized solar cells as an alternative approach to the conventional photovoltaic technology based on silicon - Recent developments in

the field and large scale applications," *Sol. Cells-ye Sensitized Devices*, pp. 471–492, 2008.

[13] D. Dodoo-arhin, Richard C. T. Howe, G. Hu,Y Zhang, P. Hiralal, A. Bello, G. Amaratunga and T Hasan, ''Inkjet-printed graphene electrodes for dye-sensitized solar cells'', *J Mater . Scie.* Carbon 105, pp. 33-41, 2016.

[14] H. Lin, C. P. Huang, W. Li, C. Ni, S. I. Shah, and Y. H. Tseng, "Size dependency of nanocrystalline TiO_2 on its optical property and photocatalytic reactivity exemplified by 2-chlorophenol," *Appl. Catal. B Environ.*, vol. 68, no. 1–2, pp. 1–11, 2006.

[15] A. L. Linsebigler, G. Lu, and J. T. Yates, "Photocatalysis on TiO_2 surfaces: principles, mechanisms, and selected results," *Chem. Rev.*, vol. 95, no. 3, pp. 735–758, 1995.

[16] S. Bose, V. Soni, and K. R. Genwa, "Recent advances and future prospects for dye sensitized solar cells: A review," *Int. J. Sci. Res. Publ.*, vol. 5, no. 1, pp. 2250–3153, 2015.

[17] E. Union and B. Laboratories, "Introduction to dye sensitized solar cells. Chapter 1, pp. 1–50.

[18] T. S. Council, "About titanium dioxide," *Titanium Dioxide Manufacturers Association* , no. 202, pp. 1–8, 2012.

[19] H. Feng, M.-H. Zhang, and L. E. Yu, "Hydrothermal synthesis and photocatalytic performance of metal-ions doped TiO_2," *Appl. Catal. A Gen.*, vol. 413–414, pp. 238–244, 2012.

[20] U. Diebold, "The surface science of titanium dioxide," vol. 48, no. x, 2003.

[21] Z. Chengli, K. Shifei, L. I. Bo, and L. I. Xi, "Photocatalytic reduction of carbon dioxide," *ACS Sustainable Chemistry & Engineering*, pp. 1–9, 1978.

[22] H. Knözinger and K. Kochloefl, "Heterogeneous catalysis and solid catalysts," *Ullmann's Encycl. Ind. Chem.*, vol. 1, pp. 2–110, 2009.

[23] A. Ibhadon and P. Fitzpatrick, "Heterogeneous photocatalysis: Recent advances and applications," *Catalysts*, vol. 3, no. 1, pp. 189–218, 2013.

[24] C. Y. Tsai, H. C. Hsi, T. H. Kuo, Y. M. Chang, and J. H. Liou, "Preparation of Cu-doped TiO_2 photocatalyst with thermal plasma torch for low-concentration mercury removal," *Aerosol Air Qual. Res.*, vol. 13, no. 2, pp. 639–648, 2013.

[25] M. De Graef and M. E. McHenry, “Crystal structure descriptions,” *Struct. Mater.*, pp. 1–101, 2012.

[26] Y. Qin and Q. Peng, “Ruthenium sensitizers and their applications in dye-sensitized solar cells,” *Int. J. Photoenergy*, vol. 2012, no. Ii, 2012.

[27] D. Sensitized, S. Cells, N. Sawhney, A. Raghav, and S. Satapathi, “Utilization of naturally occurring dyes as,” pp. 1–6, 2016.

[28] W. Ying, J. Yang, M. Wielopolski, T. Moehl, J.E. Moser, P. Comte, J. Hua, S. M Zakeeruddin, H. Tian and M Grätzel. “New pyrido[3,4-b]pyrazine-based sensitizers for efficient and stable dye-sensitized solar cells,” *Chem. Sci.*, vol. 5, no. 1, p. 206, 2014.

[29] I. U. of P. and A. Chemistry, *Nomenclature of Inorganic Chemistry: IUPAC Recomendations 2005*, 2005.

[30] A.J. Hartmann1, M. Neilson, R.N. Lamb, K. Watanabe and J.F. Scott’’ Ruthenium oxide and strontium ruthenate electrodes for ferroelectric thin-films capacitors,’’ *Appl. Phys.* A 70, pp. 239–242, 2000.

[31] T. Maekawa, K. Kurosaki, H Muta, M. Uno and S. Yamanaka’’ Thermoelectric properties of perovskite type strontium ruthenium oxide,’’ *J.Alloys Comp.*, 387, pp. 56–59, 2005.

[32] M. Yang, “Band gap engineering and carrier transport in TiO_2 for solar energy harvesting,’’ *Ph.D. University of Pittsburgh*, pp. 1-142, 2012.

[33] J. Hou and X. Guo, “Organic solar cells,” *J. Am. Chem. Soc*, 135, pp. 5529–5532, 2013.

[34] L. Dou, Y. Liu, Z. Hong, G. Li, and Y. Yang, “Low-bandgap near-IR conjugated polymers/molecules for organic electronics,” *Chem. Rev.*, vol. 115, no. 23, pp. 12633–12665, 2015.

[35] Y. Yang, “Unexpected robustness of the band gaps of TiO_2 under high pressures”, *Hefei* 230031, pp. 1–26, 2017.

[36] D. H Anjum, N.K Memon, M. Ismail, G Liu, T.C Yin, J. Wang, P. Niu, C. Zhen, Y. Xie and H.M Cheng., “A red anatase TiO_2 photocatalyst for solar energy conversion,” *Energy Environ. Sci.*, vol. 5, no. 11, p. 9603, 2012.

[37] F. Huang, A. Yan, and H. Zhao, “Influences of doping on photocatalytic properties

of TiO_2 photocatalyst,"*http://dx.doi.org/10.5772/63234*, pp. 1-80, 2016.

[38] B. Tang, H. Chen , H. Peng, Z. Wang and W. Huang, ''Graphene modified TiO_2 composite photocatalysts: mechanism: Progress and perspective''*Nanomaterials*, 8, 105, pp. 1-27, 2018.

[39] T. Morikawa, R. Asahi, and T. Ohwaki, "Visible-light photocatalyst-nitrogen-doped titanium dioxide," *R&D Rev. Toyota CRDL*, vol. 40, no. 3, pp. 45–50, 2005.

[40] J.-G. Ma, C.R Zhang, J.J Gong, Y.Z Wu, S.Z Kou, H. Yang, Y.H Chen, Z.J Liu and H.S Chen "The electronic wtructures and optical properties of alkaline-earth metals doped anatase TiO_2: A comparative study of screened hybrid functional and generalized gradient approximation," *Materials (Basel).*, vol. 8, no. 8, pp. 5508–5525, 2015.

[41] M. Haruta and M. Daté, "Advances in the catalysis of Au nanoparticles," *Appl. Catal. A Gen.*, vol. 222, no. 1–2, pp. 427–437, 2001.

[42] M. Gao, A. Lyalin, and T. Taketsugu, "CO oxidation on h-BN supported Au atom," *J. Chem. Phys.*, vol. 138, no. 3, 2013.

[43] H. Wang, Y. Liua , M. Li, H. Huang, H.m Xu, R.j Hong and H. Shena "Multifunctional TiO_2 nanowires-modified nanoparticles bilayer film for 3D dye-sensitized solar cells," *Optoelectron. Adv. Mater. Rapid Commun.*, vol. 4, no. 8, pp. 1166–1169, 2010.

[44] M. Tillotson, P. Brett, R.A. Bennett, and R. Grau-Crespo.'' Adsorption of organic molecules at the TiO_2 (110) surface: the effect of van der Waals interactions.'' *Surf. Sci.*, pp. 1-32, 2014.

[45] Z. Zhao, Z. Li and Z. Zou,'' Surface properties and electronic structure of low-index stoichiometric anatase TiO_2 surfaces'', *J. Phys: Condens Matter*, vol 22, no 17, 2010.

[46] J. Muscat, V. Swamy, and N. M. Harrison, "First-principles calculations of the phase stability of TiO_2," *Phys. Rev. B - Condens. Matter Mater. Phys.*, vol. 65, no. 22, pp. 2241121–22411215, 2002.

[47] L. Triggiani, A. B. Muñoz-García, A. Agostiano, and M. Pavone, "First-principles study of trimethylamine adsorption on anatase TiO_2 nanorod surfaces," *Theor. Chem. Acc.*, vol. 134, no. 10, pp. 1–11, 2015.

[48] A. Fujishima and K. Honda, "TiO_2 photoelectrochemistry and photocatalysis," *Nature*, vol. 213, no. 1998, p. 8656, 1972.

[49] A. Fujishima and K. Honda, "Electrochemical photolysis of water at a semiconductor electrode," *Nature*, vol. 238, no. 5358, pp. 37–38, 1972.

[50] Q. Chen, C. Tang, and G. Zheng, "First-principles study of TiO_2 anatase (1 0 1) surfaces doped with N," *Phys. B: Condens. Matter*, vol. 404, no. 8–11, pp. 1074–1078, 2009.

[51] D. Yu, W. Zhou, Y. Liu, B. Zhou, and P. Wu, "Density functional theory study of the structural, electronic and optical properties of C-doped anatase TiO_2 (101) surface," *Phys. Lett. Sect. A Gen. At. Solid State Phys.*, vol. 379, no. 28–29, pp. 1666–1670, 2015.

[52] A. Navrotsky, "Nanoscale effects on thermodynamics and phase equilibria in oxide systems," *Phys. Chem.*, vol. 12, no. 12, pp. 2207–2215, 2011.

[53] W. Chen, Q. Kuang, Q. Wang, and Z. Xie, "Engineering a high energy surface of anatase TiO_2 crystals towards enhanced performance for energy conversion and environmental applications," *RSC Adv.*, vol. 5, no. 26, pp. 20396–20409, 2015.

[54] T. R. Esch, I. Gadaczek, and T. Bredow, "Surface structures and thermodynamics of low-index of rutile, brookite and anatase - A comparative DFT study," *Appl. Surf. Sci.*, vol. 288, no. October 2017, pp. 275–287, 2014.

[55] R.O. Jones and O. Gunnarsson, ''The density functional formalism, its applications and prospects'', *Rev. Mod. Phys*. 61, 689 1989.

[56] U.V. Barth,'' Basic density-functional theory an overview,*'' Physica Scripta*. vol. T109,pp. 9–39, 2004.

[57] Capelle K., "A bird's-eye view of density-functional theory," *Cond. Mat. Mater. Sci.*,pp. 1–59. 2006.

[58] G Eğilmez**,** G.A. Süer and O Özgüner**.** "World largest Science , Technology & Medicine Open Access book publisher :," *Des. Control Appl. Mechatron. Syst. Eng.*, pp. 135–152, 2012.

[59] S. Cottenier, Density functional theory and the family of (L)APW-methods: a step-by-step introduction,'' *Center for Molecular Modellimg and Department of Materials Science and Engineering,* pp.1-75, 2013.

[60] S. Sharma, T. Yanai, G. H. Booth, C. J. Umrigar, and G. K Chan. “Introduction to density functional Theory,” *J. Chem. Phys,* A 109, 11127, 2005.

[61] C. Filippi, C. J. Umrigar, and X. Gonze, “Separation of the exchange-correlation potential into exchange plus correlation: An optimized effective potential approach,” *Phys. Rev. A - At. Mol. Opt. Phys.*, vol. 54, no. 6, pp. 4810–4814, 1996.

[62] A. T. B. Gilbert and P. M. W. Gill, “Decomposition of exchange-correlation energies,” *Chem. Phys. Lett.*, vol. 312, no. 5–6, pp. 511–521, 1999.

[63] H. Vesa, “Introduction to computational chemistry,” pp. 1–20, 2012.

[64] S. I. Uchida, “High temperature superconductivity: The road to higher critical temperature,” *Springer Ser. Mater. Sci.*, vol. 213, pp. 7–17, 2014.

[65] L. He, “Accuracy of generalized gradient approximation functionals for density-functional perturbation theory calculations,” *Phys. Rev. B - Condens. Matter Mater. Phys.*, vol. 89, no. 6, pp. 1–16, 2014.

[66] C. Skylaris, “CHEM6085 : Density functional theory lecture 9 Exchange-correlation functionals Kohn-Sham energy expression,” *Univ. Southampton,* 1989.

[67] K. Refson, *Introduction to DFT and the plane-wave pseudopotential method*’’, *Science and Technology facilities council*, 1-55, 2014.

[68] S. Tewari, “The energy bands for palladium by the augmented-plane-wave method,” *Solid State Commun.*, vol. 11, no. 9, pp. 1157–1160, 1972.

[69] E. Wimmer, “The growing importance of computations in materials science. Current capabilities and perspectives,” *Mater. Sci. Pol.*, vol. 23, no. 2, pp. 325–345, 2005.

[70] C. M. Physics, “Lecture 6 – Bloch ’ s theorem,” *Reading*, pp. 2–4, 2009.

[71] F.-X. Coudert, “DFT with plane waves , pseudopotentials,” *Tutoriel CPMD/CP2k*, p. 22, 2010.

[72] E. J. Bylaska, “Introduction to plane-wave basis sets and pseudopotential theory’’, *J.Phys.Chem*, 100, 6966, 1996.

[73] G. Kresse and D. Joubert, ‘’Ultrasoft pseudopotentials to the projector augmented-wave method. *Phys. Rev. B*, 59, 1758-1775, 1999.

[74] W. Walkosz, “Atomic scale characterization and first-principles studies of Si_3N_4 interfaces,” *Academic Press,* pp. 11–22, 2011.

[75] L. Prepared, C. R. King, and T. Ece, “Density of states : 2D, 1D and 0D,” *Slides*,

2005.

[76] M. C. Payne, M.P. Teter, D.C. Allan, T.A. Arias and J.D. Joannopoulos,'' Iterative minimization techniques for ab initio total-energy calculations: molecular dynamics and conjugate gradients''. *Rev. Mod. Phys*. 1992, 64, 1045.

[77] L. Lyu, "Chapter 3 . Pseudopotential methods," no. I, pp. 1–31, 2005.

[78] L. O. Jay, H. Kim, and J. R. Chelikowsky, "Electronic structure calculations In plane-wave codes without diagonalization*," Kluwer Academic Publishers*, pp. 1–10, 1996.

[79] P. B. Allen,'' Introduction to Pseudopotentials and Electronic Structure'', *Stony Brook University* ,3, 2014.

[80] J. M. Carlsson, "Pseudopotentials : From ultrahard to ultrasoft," vol. 604, 1967.

[81] S. J. Clark *et al.*, "First principles methods using CASTEP," *Zeitschrift für Krist.*, vol. 220, no. 5-6–2005, pp. 567–570, 2005.

[82] J. D. Pack and H. J. Monkhorst, "'Special points for Brillouin-zone integrations'- a reply," *Phys. Rev. B*, vol. 16, no. 4, pp. 1748–1749, 1977.

[83] A. Eichler, "Sampling the Brillouin-zone :," *PowerPoint*, pp. 1–31, 2005.

[84] M. Guo and J. Du, "First-principles study of electronic structures and optical properties of Cu, Ag, and Au-doped anatase TiO_2," pp. 1–12, 2012.

[85] Y. Wang, R. Zhang, J. Li, L. Li, and S. Lin, "First-principles study on transition metal-doped anatase TiO_2," *Nanoscale Res. Lett.*, vol. 9, no. 1, pp. 1–8, 2014.

[86] S. Khaleghi, "Calculation of electronic and optical properties of doped titanium dioxide nanostructure," *J. Nanostructures*, vol. 2, pp. 157–161, 2012.

[87] T. S. El-Shazly, W. M. I. Hassan, S. S. A. Rehim, and N. K. Allam, "DFT insights into the electronic and optical properties of fluorine-doped monoclinic niobium pentoxide (B-Nb_2O_5:F)," *Appl. Phys. A Mater. Sci. Process.*, vol. 122, no. 9, 2016.